View metadata, citation and similar papers at core.ac.uk
brought to you by CORE
provided by UPCommons

Universitat Politècnica de Catalunya
Escola Tècnica Superior de Enginyeria de Telecomunicació de Barcelona
Department of Electronics

Jaime Arroyo Pedrero

Dielectric characterization for hot film anemometry in METNET Mars Mission

Final Project

Director: Dr. Luis Castañer Muñoz
Supervisor: Jordi Ricart Campos
Barcelona, January 18, 2010

Preface

This Final Project has been carried out in the Department of Electronics at the Universitat Politècnica de Catalunya (UPC) during 2009 under the direction of Luis Castañer Muñoz and the supervision of Jordi Ricart Campos.

I would like to thank specially Jordi Ricart for his important dedication to me and this thesis patiently teaching me to make use of the clean room, all the specific equipment needed during the development of the present work and the techniques and procedures involved. It has been a long journey since I first entered the clean room until I felt comfortable carrying out my research which it would have been impossible without his guide.

I also owe gratitude to professor Luis Castañer which helped me in the first stages to understand the real challenge which represents Mars exploration to human development and this particular design problem. Hence he allowed me to choose the correct scope according not only to the needs of the project but also to my own interest. Furthermore his experience has been priceless regarding the format and correctness of the present report.

Similarly, I give thanks to Lucasz Kowalski for his theoretical explanations with regard to thermal circuits and some fluid dynamics concepts.

I want to mention also Gema López and the technical staff of the clean room whose assistance during my work at it, has softened the various problems appeared.

I am also grateful to my colleague Samir Kassar which contribution and work has been necessary as starting point to this thesis. Indeed, I thank Jordi Amorós and David López who have shared time and the same working space, and helped me during the development of this thesis.

Last but not least, I would like to give my warmest thanks to my parents, Casto and Conchita, and my sister Adelia, for supporting me from the beginning until the end in different circumstances. The same for my friend Carolina who is always there to ensure I afford all my tasks in life with the convenient excellency and dedication.

Huge thanks go to all of you and to the ones I have not mentioned by name in this preface.

January 18, 2010
Jaime Arroyo Pedrero

Contents

1 Introduction **4**
1.1 MetNet Mars mission . . . 4
1.1.1 Science objectives . . . 5
1.1.2 Meteorological boom . . . 7
1.2 Mars atmosphere . . . 8
1.2.1 Atmosphere composition . . . 8
1.2.2 Winds . . . 9
1.3 Wind speed measurements in Mars atmosphere . . . 10
1.4 Objective of this work . . . 12

2 Theoretical Background **14**
2.1 Thermal anemometry . . . 14
2.2 Fabrication Technology . . . 24
2.2.1 Sputter Deposition . . . 25

3 Sensor development **27**
3.1 Previous developments . . . 27
3.1.1 REMS . . . 27
3.2 Prototype . . . 29
3.3 Isolation materials . . . 36
3.3.1 Silicon Oxide . . . 36
3.3.2 Aluminum Nitride . . . 37
3.3.3 Carbon Nitride . . . 39
3.4 Further work . . . 40

4 Characterization **41**
4.1 Thickness measurements . . . 41
4.2 Thermal measurements . . . 43
4.2.1 Silicon Wafer depositions . . . 44
4.2.2 Teflon depositions . . . 46
4.3 Electrical measurements . . . 47
4.3.1 Electrical Resistivity . . . 47
4.3.2 Open loop test . . . 48

4.3.3 Closed-loop validation 49

5 Results and discussion **51**

6 Summary and Conclusions **62**

A Virtual Instruments **69**

A.1 Thermal Measurements 70

A.2 Close Loop Validation 71

Chapter 1

Introduction

In this first introductory chapter, the scientific context of the work will be presented as well as its main objectives. Briefly, the purpose of the work is to develop a very specific part of the wind speed sensor which is being developed to the *MetNet* Mars Mission: an electrically isolating layer which interfaces the sensor device itself with the surrounding environment (air).

The different aspects of the work have been presented from a general to a more concrete perspective. Hence, we start with an overview of the most relevant characteristics of the MetNet project. Subsequently, the Mars atmosphere is introduced in order to better understand the challenges implied in the development of a wind speed sensor for such environment. Its composition is analyzed and, also, its main metereological phenomena are described. After this, previously used techniques in Mars for wind speed measurement are explained as well as the predecessor of the current design, REMS.

Finally, the objectives of this work are detailed. Those include the bibliographic research carried out, the fabrication process verification performed, the different material characterized, and the final validation of the overall functionality.

1.1 MetNet Mars mission

The *MetNet* (Meteorological Network) Mars Mission is a wide-spread surface *in situ* observational network and orbital platform mission around Mars to investigate its atmospheric structure, physics and meteorology. That is, the mission includes sending several (up to 20) *MetNet Landers* (MNL) on the Martian surface and one *MetNet Orbiter* (MNO). Although MetNet development started on 2001 by the Finnish Meteorological Institute (FMI) who defined and initiated the mission, it is the successor of the *NetLander* Mission's atmospheric part and is also the continuation of the Russian *Mars 96* Mission. The *MetNet* Mars Mission (MMM) is to be implemented in collaboration with:

1. European Space Agency (ESA), in the framework of the first planning cycle of Cosmic Vision 2015-2025.

2. Finnish Meteorological Institute (FMI), mission and payload lead.
3. Russian Space Research Institute (IKI), payload lead.
4. Lavochkin Association (LA) - Babakin Space Center, systems lead.
5. Instituto Nacional de Técnica Aeroespacial (INTA), provides part of the payload.

It consists of the development of at least 16 *MetNet Landers* (MNLs) and its deployment on the surface of Mars by means of an inflatable descent system. In addition, they will be accompanied by an atmospheric sounder, onboard the *MetNet* Orbiter (MNO), that will serve as the primary data relay between the MNLs and the Earth.

The MNL is a new semi-hard landing vehicle and will be able to resist a shock against the Martian surface of at least 500 times the earth gravitational force for 50ms. The descent vehicle will consist of the use of state-of-the-art inflatable systems. This way the reliability is increased because of the less number of pyrotechnical devices needed in previously used rigid heat shields and parachutes.

The MNL and other critical subsystems have been fully qualified for Martian environment. Development of a precursory mission (called *Mars MetNet Precursor Mission*,MMPM) is under way and launch is planned for 2011 after being delayed (It was originally planned for October 2009). The precursory mission will consist of one lander and is intended as a technology and science demonstration mission. More landers will be deployed in the following launch windows extending up to 2019.

1.1.1 Science objectives

Since meteorological and climatological phenomena have both temporal and spatial variations in scales ranging from local to global and from daily to annual (See Section 1.2), characterization of such phenomena requires ideally simultaneous observations at multiple locations and over a sufficiently long period of time. Hence a surface network combined with an orbiting sounder is the best feasible means of observation. The observation posts should be located on areas with variable types of geography, terrain, thermal inertia, altitude, surface materials, albedo, etc. At least ten to twenty observation posts are required to address planet-wide atmospheric phenomena.

The ultimate objectives of MMM are to provide support for the safety of the forthcoming Mars mission elements, retrieving weather data and gaining accurate knowledge of atmospheric conditions (See Table 1.1). Improve the understanding of mesoscale phenomena (B-1) such as CO_2 cap edge circulations, slope winds, etc, will help choosing priority landing sites form a future programmatic perspective (human missions, etc.). Hence, its payload instruments are focused on the atmospheric science of Mars:

1. Primary scientific objectives related with characterization of various meteorological phenomena on Mars to provide a deeper understanding of the Martian climate (A).

Science Objectives	
Primary scientific objectives	Additional Scientific objectives
A-1 General circulation and climatological cycles.	B-1 Mesoscale phenomena.
A-2 Planetary boundary layer and surface-atmosphere interactions.	B-2 Future missions.
A-3 Atmospheric vertical structure.	B-3 Ground truth for other missions.
A-4 Condensation clouds.	
A-5 Martian internal structure and composition.	

Table 1.1: Objectives of the *MetNet* Mars Mission, according to [1].

2. Additional scientific objectives related to obtain *in situ* data at all levels to help future missions involving humans. This involves both atmospheric data and ground research such as seismic and magnetic measurements (B).

To sum up, the MetNet mission goal is to comprehensively address this objectives by means of deploying a primarily global-scale, multi-point surface observation network supplemented by an orbiting atmospheric remote sounder operating at least for two Martian years.

Thus, during the entry and the descent phase, an instrument package composed of an imager, 3-axis accelerometers and devices for flow pressure and temperature observations will be used. These measurements will provide vertical profiles (A-3) of the atmospheric pressure, temperature, H_2O, etc. The orbiting sounder (MNO) will in turn provide (less accurate) continuous and long-term data to complete these profiles.

Once on the Martian surface, the MNL will take panoramic pictures, perform measurements of pressure, temperature, humidity, wind speed and direction, atmospheric optical depth, dust and other aerosols, and low altitude clouds. They will provide information related with global circulation and climate (A-1) as well as characteristics of the condensation clouds (A-4).

Furthermore, the *atmospheric boundary layer* (ABL) phenomena will be studied analyzing the dependence between the varying surface characteristics of the large number of landing sites and its atmospheric interaction (A-2). Ground and atmospheric temperature, high resolution wind data and humidity measurements, will be used to estimate stability, surface fluxes of momentum, heat and growth of the mixed layer, etc.

Finally, gravity data, analysis of meteoroids, seismological and magnetic observations will shed light on the internal structure and composition of the planet (A-5). Indeed, other ground data such surface pressure could help to improve accuracy of other model-based remote sensing measurements of the Mars Landers or other missions (B-2).

MetNet Payload		
Atmospheric Instruments	Optical Devices	Composition and Structure Devices
Pressure Instrument (*MetBaro*)	Panoramic Camera (*PanCam*)	Tri-axial Magnetometer (*MOURA*)
Humidity Device (*MetHumi*)	Solar Irradiance Sensor (*MetSIS*)	Accelerometer
Temperature Sensors	Dust Sensor (*DS*)	
Wind Sensor		

Table 1.2: According to [1], FMI provides: MetBaro and MetHumi. IKI provides: Accelerometer, Temperature Sensors and PanCam. INTA provides: MetSIS, DS and MOURA. Finally, MNT (Department of Electronics, UPC) provides the Wind Sensor.

1.1.2 Meteorological boom

The MNL contains a 90 cm long boom which is deployed after the landing as can be observed in Figure 1.1. It is of interest since it will be the carrier of the wind speed sensor partly developed in this work. Thus, it provides supports and attachment points at enough height from the surface for the allocation of the wind sensor within other equipment such as the antenna, a panoramic camera, the humidity sensor and temperature sensors (See Table 1.2 to see all the payload onboard the MNL). However not all the MetNet payload is located at the boom. Only those instruments highly interactive with air or those which need some height to work. For example, the accelerometer, the barometer or the magnetometer are not located on the boom.

The boom is manufactured from ceroplastic (a carbon composite) to ensure a minimum structural weight. It consists of three joints, which are stacked inside the *Shock Absorption System* (SAS) container during the flight, entry, descent and landing reducing shock requirements from 1200 times the gravitational force (actual shock kinetic force) to a more permissible value of 400. The SAS is, in turn, inside the *Payload Bay* which is located in the core of the MNL body and works as the cover for the most of the scientific devices and other payload systems.

After landing the boom is deployed in a vertical orientation with a command from the probe control system. The deployment mechanism consists of springs with clamps which provide rigidity for the structure after deployment.

The wires that communicate with the sensors pass through the boom which is hollow. It therefore provides mechanical protection for the cables during operation. It is covered with white dim enamel to achieve minimal radiation overheating and disturbance of measurements and hence ensuring good optical properties.

Finally, the antenna, located at the top of the boom, is a variant of the asymmetrical dipole antenna with a coaxial feed line. The design of the antenna tried to decouple its impedance from physical parameters of the surface at the landing place.

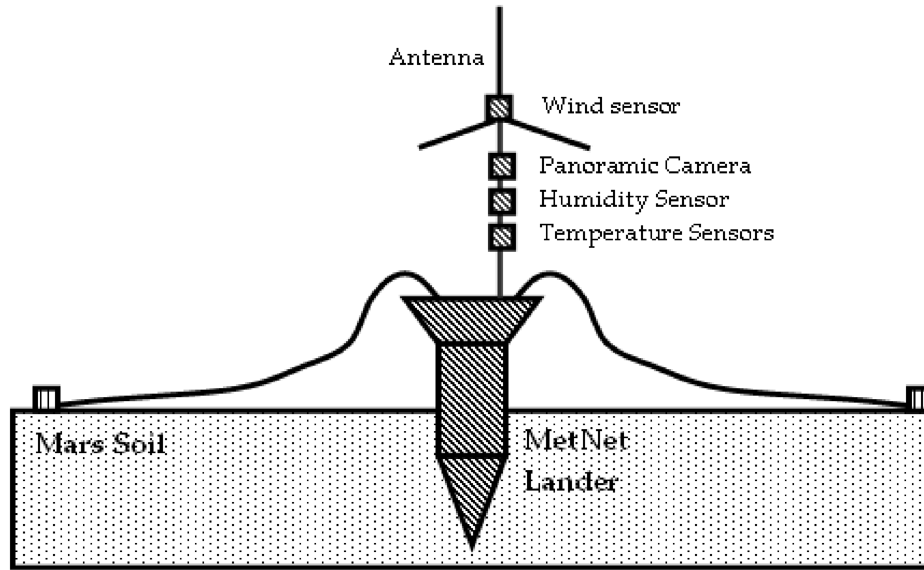

Figure 1.1: Schematic plot of the boom deployment over the MNL after landing at Mars surface.

1.2 Mars atmosphere

A Mars day is only 37 minutes and 22 seconds longer than an Earth day. The obliquity, that is, the angle between the equatorial plane and the orbital plane is of 25.2º for Mars, close to the one of Earth which is 23.4º. In addition, there are also four seasons, but their cycle lasts for 669 Martian days, about 687 Earth days. However, the cycle of seasons is much more marked due to the mars surface.

Martian soil is dry and granular and therefore it hardly stores heat: its *thermal inertia* is very low compared to the Earth oceans. Indeed, its tenuous atmosphere (see Section 1.2.1) makes variations much more marked. Hence during solstices most solar energy is received by the pole pointing the sun, which lacks the reflectivity of ice, being then the polar region of the summer hemisphere the hottest part of the planet at the solstice. On the other hand, at Martian equinoxes, polar regions are cold, and the equator is warm.

1.2.1 Atmosphere composition

Thanks to the Mariner (1965), today we know that, compared to the Earth, the atmosphere of Mars is very tenuous, with a mean surface pressure of around 6 hPa at the surface (about 1% of the pressure at the Earth which is 1013.25 hPa). It consists of 95% carbon dioxide (CO_2) which make it unbreathable to humans. The rest of components were determined by the Viking probe (1976) were *in situ* measurements were performed. Thus, the presence of nitrogen (N_2) and argon (Ar) were confirmed as well as oxygen (O_2), in negligible proportion compared to the Earth. Finally, other rare gases were found such as neon (Ne), krypton (Kr) and xenon (Xe) (less than 5 ppm) within other elements (See the

complete composition at Table 1.3).

Despite the fact that extreme ultraviolet radiation photos are absorbed by few molecules present at the thermosphere (over 120km up), since Mars has negligible ozone (O_3) protection from ultraviolet radiation, this radiation reaches the CO_2, between 60km and 120km up, dissociating it into molecules of O_2 and carbon monoxide (CO). However, due to the scarcity of water vapour, there is OH, a reactive agent, which accelerates the oxidization of CO and recombines with O_2 back into CO_2. Thus, the quantity of CO and O_2 remains small compared to the amount of CO_2.

During the Martian winter the poles are in continual darkness freezing as much as a quarter part of the total amount of atmospheric CO_2 which condenses at the polar caps into dry ice. When the poles are again exposed to sunlight during Martian summer, the CO_2 sublimes back into the atmosphere which leads to a significant variation of both the atmospheric pressure and composition on a yearly basis, near the poles.

1.2.2 Winds

Atmospheric circulation, both in Mars and the Earth, is caused by two combined mechanisms:

1. Thermal differences.
2. The Rotation of the planet.

Thermal differences are created by solar irradiation which in turn makes the air move. On one hand, warm air expands and rises creating pressure difference at altitude. On the other hand, masses of air at higher pressures are pushed towards low-pressure (cooler) regions. This effect is known as meridional north-south circulation or *Hadley circulation*, after the English physicist who first described the process in 1735 (See Figure 1.2). While on Earth, the atmosphere forms pair of *cells* between the intertropical zone and each of the hemispheres, on Mars, only one large Hadley cell forms, which is much more developed at altitude (up to 50km compared to 20km on Earth).

Near the surface, at the base of the ascending part of the Hadley cell, the air follows the rotation of the planet on its axis. Nevertheless, when air masses are transported to the Equator, in the upper part of the cell, they move away from the axis of rotation because they tend to turn around slower than the planet, creating winds in the opposite direction, that is, blowing from east to west. As the air masses approach to the pole, they become nearer to the rotational axis as well. They will then turn faster than the planet, to form a strong westerly jet around the pole, analogous to the terrestrial *jet stream*.

With respect to the other mechanism of wind formation, it is deduced from the data available mostly thanks to the Viking landers, that air movements due to planetary rotation are not much different from those observed in Earth, that is, jet stream, trade winds, etc. Hence Mars, as the earth, has westerly winds at around 50°N. However, some fundamental differences arise due to the absence of oceans on Mars. Therefore, if in the Earth the lower layers of the atmosphere are generally warmer at the tropics than at the poles, in Mars

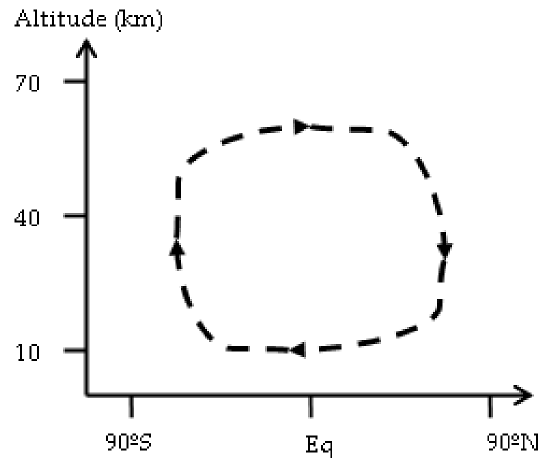

Figure 1.2: Hadley circulation. It can be seen the flow of the air masses through the mars surface (horizontal axis) and the altitude (vertical axis).

the thermal contrast is between the summer hemisphere and the winter hemisphere which is enhanced because of the dusty atmosphere, much more absorbent of solar radiation. Around the equinoxes, however, Mars behaves in a more Earth-like way, because poles are colder at that time.

1.3 Wind speed measurements in Mars atmosphere

Wind speed measurements can be performed in a number of ways. It must be taken into account the particular case of the Mars atmosphere which is predominantly made of CO_2 with a very low density of 6 mbar in average (See Section 1.2). Further, it presents a wide range of temperatures (-125 to +25°C), fast temperature and wind speed changes, and dust particles are present during storms. Nonetheless, several methods have been described to measure wind speed in Mars conditions including:

1. Ion drift: A gas-discharge anemometers based on the phenomenon of gas-flow-induced deflection of a weak-current low-energy ion beam. The glow discharge is used for producing an ion beam. According to [2], a sensitivity of 100 mV/m/s can be achieved.

2. Laser: laser-based anemometers measure suspended dust grain velocity and turbulence. It is insensitive to contamination or atmospheric conditions such as temperature, pressure or composition [3].

3. Windsocks: A low-mass component of the *Imager Mars Pathfinder* (IMP) investigation that allowed measurement of the wind profile on the Martian surface. Thus, the windsock deflection angle θ and wind azimuth Φ is obtained from information concerning IMP pointing recorded during windsock imaging, and the direction of lander tilt measured by onboard accelerometers [4].

Compound	Mars	Earth
Carbon dioxide CO_2	95.32%	0.035%
Nitrogen N_2	2.7%	78%
Argon Ar	1.6%	0.93%
Oxygen O_2	0.13%	20.6%
Carbon monoxide CO	0.07%	0.00002%
Water vapour H_2O	0.03%	0.04%
Nitric Oxide NO	0.013%	0%
Neon Ne	2.5ppm	18.8ppm
Krypton Kr	300ppb	1.14 ppm
Methanol CH_2O	130 ppb	
Xenon Xe	80ppb	0.09 ppm
Ozone O_3	30 ppb	0.07 ppm
Methane CH_4	10.5 ppb	1.745 ppm

Table 1.3: Principal constituents of Mars atmosphere and their relative concentration compared to the Earth.

4. Tell-tales: consist of a light-weight cylinder that swings out due to wind action. Images taken of the experiment gives information on wind speeds and direction. The telltale is heighted 10 cm and is designed to work at the low atmospheric pressure. It is mounted on top of the meteorological mast and a mirror will help in determining wind directions [5].

5. Thermal anemometers such as hot wire anemometry which were incorporated in *MPL/Netlander*, *Pathfinder* and *Beagle2*. This technique has been successfully demonstrated during the Viking mission and benefits from a general simplicity and robustness. However, they are sensitive to pressure, gas composition, air temperature, and their own overheating which may induce systematic errors. See [6],[7], [8] and [9].

Among the methods introduced so far, a particularly relevant precedent of wind speed measurement for this thesis is the wind sensor which has been included in the *Mars Science Laboratory* (MSL), onboard the *Rover Environment Monitoring Station* (REMS), which will be launched in 2011 after being delayed [10]. It consists of a 2D hot film anemometer composed of four hot points and a reference point that uses a closed thermal feedback loop based on thermal sigma-delta modulation. Platinum resistors were used improving thermal isolation [11]. Thus, its main properties are:

1. A hot point die which is composed of three platinum resistors defined by photolithography on top of an oxidized silicon wafer.

2. Those resistors measure the local temperature, heat the die and set a operating difference of temperature with the closed-loop controller.

3. A electro-thermal sigma-delta which closes the loop and provides direct digital readout of the thermal conductance.

4. An arrangement which consists of a square array of four hot dice and a cold reference die and allows the computation of the angle of incidence of the wind flow.

5. Sensitivity of around 0.3 m/s in wind speed and 10° in angle.

1.4 Objective of this work

In a few words, the main purpose of this work has been the *research, fabrication, characterization and testing of a material with the suitable properties to work as an interface layer between a hot film anemometer and its surrounding air.* After explaining the working principle of the anemometer the suitable features of the idealistic material will be justified. These are:

1. Electrical insulator: High electrical resistivity.

2. Thermal conductor: High thermal conductivity.

In fact, there were some constraints to the selection, so to speak. The fabrication technology, in other words, the process of deposition had to be sputter deposition (See Section 2.2.1), which is carried out almost at room temperature, in order to reduce the impact of such process over the rest of the wind sensor. This is because low temperature process is compelling to test the reliability of the design concept over a plastic ball (See Section 3.2).

Considering the availability of *target* materials, and after a bibliographic research four candidates were chosen (two oxides and two nitrides):

1. Oxides

    (a) Silicon Dioxide SiO_2. It was selected as a reference material with very well known properties. Hence it was the worst case scenario selection.

    (b) Tin Dioxide SnO_2. There have been previous experimentation with this material in the clean room of the department. Hence process parameters were known in advance. It was considered as a first alternative but, as shown later, consistently with bibliographic resources, its properties were not suitable.

2. Nitrides

    (a) Carbon Nitride CN_X. As long as overwhelming properties of diamond perfectly matched our needs, similar materials (known as diamond-like materials) were investigated. This one turned out to be a great option. However, its sputter fabrication is relatively recent and it seemed to involve difficulties to achieve proper stochiometries such as the super hard *Beta carbon nitride* ($\beta - C_3N_4$).

(b) Aluminum Nitride. This option is a typically used electrical insulator (within others such as SiO_2, Al_2O_3, Ta_2O_5, Si_3N_4, see for instance, page 465 of [12]) and it turned out to have, theoretically, the best thermal properties of those.

The main goal of the project is therefore to figure out which is the best material. Accordingly, several experiments will be made to check the properties of each one. Besides, the election has to be made so that the previous developments of the sensor are still valid and the overall functionality is improved. To ensure this, it has to be made a closed-loop validation that will complete the work.

Finally, it is important to point out that it is well beyond the scope of the present work to perform a scientific characterization of materials. On the contrary, it is a qualitative characterization only meant to overtake a specific engineering problem.

Chapter 2

Theoretical Background

In this chapter, most relevant theoretical aspects of the work performed in this thesis are presented. First of all, Hot-wire/film anemometry is studied, starting from a general point of view to the most relevant specific aspects related to this work such as the dynamic response, materials, and protective coatings. Secondly, the *Physical Vapor Deposition* (PVD) technique called *Sputtering* is presented and explained.

In many cases, the importance of the analysis carried out in this chapter will not be clarified until further considerations in this report. For instance, parameters such as *thermal conductivity* and *specific heat capacity* will be key points of the discussion in next chapters of this report.

2.1 Thermal anemometry

Hot-wire anemometry is a versatile technique used for investigations in turbulent flows such as air, water, etc. It can be used, for example, for the measurement of velocity and temperature fluctuations in the time domain over wide speed ranges and from subsonic to high supersonic flows. The very small hot-wire thermal inertia allows the detection of turbulent perturbations with a large bandwidth (fast dynamic response), using the appropriate design.

Steady Analysis

Hot-wire anemometry is based on convective heat transfer from a heated wire or film element placed in a fluid flow. Any change in the fluid flow condition that affects the heat transfer from the heated element will be detected virtually instantaneously by hot wire anemometry system. This technique can therefore be used to provide information related to not only the velocity and temperature of the flow, but concentration changes in gas mixtures, and phase changes in multi-phase flows [13].The sensor is made with a material whose electric resistivity depends on the temperature. Heat is introduced in the sensor by *Joule* heating at a heating range of $R_W I_W^2$ (being I_W the current intensity in the sensor and R_W the sensor resistance when heated) and when the wire/film is dipped into a flow, it is

cooled, that is, its heat is lost primarily by forced convection at a cooling rate of the form $(T_W - TA)\phi_{conv}(U...)$ (being T_W the temperature of the wire/film when heated, T_A the temperature of the wire at the same location when unheated, or simply the temperature of the surrounding fluid when this is liquid or low subsonic gas flow, and $\phi_{conv}(U...)$ a function that mainly depends on flow velocity U, changing its electrical resistance $R(T)$ according to the Eq. 2.1 in its linear range around the operating point:

$$\begin{aligned} R_W &= R_0(1 + \chi(T_W - T_0) \\ R_A &= R_0(1 + \chi(T_A - T_0)) \end{aligned} \tag{2.1}$$

R_0 is the resistance at the *reference temperature* (293K) T_0 and $T_W - T_0$ or $T_A - T_0$ the increment of the operating point temperature (heated temperature T_W or ambient temperature T_A) with respect to the reference temperature T_0. χ is the *temperature coefficient of resistivity*, the parameter that relates resistance and temperature.

Consider a wire that is immersed in a steady fluid flow. Assume that the wire, heated by an electrical current input, is in thermal equilibrium with its environment. The heat balance between the heating and cooling rates expresses that the electrical power input is equal to the power lost due to convective heat transfer,

$$I^2 R_W = \chi_{conv}(U)(T_W - T_A) \tag{2.2}$$

A significant parameter that controls the operation of the sensor is the relative difference in resistance $(R_W - R_A)/R_A$. It is called *overheat ratio* of the sensor and is simply denoted by,

$$a_W = \frac{R_W - R_A}{R_A} \tag{2.3}$$

The value of this parameter use to be in the range from 0.05 to 1.0. Beyond this value, the sensor could be permanently deformed or oxidized.

In subsonic air flows, when forced convection prevails and the hot-wire is long (l/d in the range 2000-8000, being l the longitude and d the diameter of the wire), a dimensionless analysis leads to this expression of the heat balance (Eq. 2.2):

$$Nu = (A_N + B_N Re^n)\left(\frac{T_W + T_A}{2}\right)^m \tag{2.4}$$

where Nu is the *Nusselt* number defined as:

$$Nu = \frac{hd}{k} = \frac{R_W I_W^2}{\pi l k (T_W - T_A)} \tag{2.5}$$

where h is the *convective heat transfer coefficient* which is defined as $h = \frac{R_W I_W^2}{(T_W - T_A)A}$, being A the surface of contact, and d a *characteristic length* of the sensor (the diameter of the

wire in this case). Thus, based on the wire longitude l, $A = \pi dl$, and k is the thermal conductivity of the flow involved. Re is the *Reynolds* number of the form:

$$Re = \frac{\rho U d}{\mu} \tag{2.6}$$

where ρ is the density of the fluid, μ its Newtonian coefficient of dynamic viscosity, d the diameter of the wire and U the incident flow velocity. Finally, A_N and B_N are constants, n varies slightly around 0.5 and m sets the flow distortion around the wire caused by the addition of heat (temperature loading). The value of the constants are given by [14] for the particular case where the temperature loading is neglected ($m \cong 0$) and $2.5 \leq Re \leq 1475$:

$$Nu = 0.39 + 0.51 Re^{0.5} \tag{2.7}$$

From these expressions a practical relation which establishes the rate between power injected $R_W I_W^2$ and resistance variation $\Delta R = R_W - R_A$ as a function of flow velocity can be deduced. If we now take the equation 2.7 and substitute Nu and Re by its definition:

$$\frac{R_W I_W^2}{\pi lk(T_W - T_A)} = 0.39 + 0.51 \left(\frac{\rho U d}{\mu} \right)^{0.5} \tag{2.8}$$

Mixing both equations 2.1 to obtain the relation $T_W - T_A = \frac{R_W - R_A}{R_0 \chi}$ and reordering equation 2.8 using that expression:

$$\frac{R_W I_W^2}{R_W - R_A} = 0.39 \frac{\pi lk}{R_0 \chi} + 0.51 \frac{\pi lk}{R_0 \chi} \left(\frac{\rho d}{\mu} \right)^{0.5} U^{0.5} \tag{2.9}$$

called *King's Law* when both adding terms are grouped in new constants $A = 0.39 \frac{\pi lk}{R_0 \chi}$ and $B = 0.51 \frac{\pi lk}{R_0 \chi} \left(\frac{\rho d}{\mu} \right)^{0.5}$ such that:

$$\frac{R_W I_W^2}{R_W - R_A} = A + B U^{0.5} \tag{2.10}$$

Thus, the flow velocity can be directly deduced from electrical magnitudes:

$$U = \left(\frac{\frac{R_W I_W^2}{R_W - R_A} - A}{B} \right)^2 \tag{2.11}$$

Although A and B can be theoretically deduced from the expressions shown before, they are normally determined by calibration of the particular circuit configuration.

Dynamic analysis

When thermal energy is unsteadily stored in the wire ($\frac{dT_W}{dt} \neq 0$), the instantaneous heat balance of Eq 2.2 has to be changed to include the surplus between the outgoing and the incoming energy:

$$m_W c_W \frac{dT_W(t)}{dt} = R_W I_W^2 - \phi_{conv}(T_W(t) - T_A) \tag{2.12}$$

Where m_W i the wire mass and c_W is the *specific heat capacity* of its material. It should be noted here that R_W and ϕ are also time dependent, because their values depend on the temperature. Hence this would lead to an unlinear equation not easy to solve. However, as a first approximation, they will be considered constant which is equivalent to use the zero order Taylor expression at the working point. Hence this analysis makes sense around it (small fluctuations). To do this, we will set a working temperature T_{W0} and a working sensor resistance R_{W0} which is used to set the working value of the convection function ϕ_{conv0} and therefore simplify the equation in a first order differential equation with constants coefficients:

$$\phi_{conv0} = \frac{R_{W0} I_W^2}{T_{W0} - T_A} \tag{2.13}$$

Now, we can remove χ_{conv} from the balance equation 2.12:

$$m_W c_W \frac{dT_W(t)}{dt} = R_{W0} I_W^2 - \frac{R_{W0} I_W^2}{T_{W0} - T_A}(T_W(t) - T_A) \tag{2.14}$$

Reorganizing the equation we obtain:

$$m_W c_W \frac{dT_W(t)}{dt} + \frac{R_{W0} I_W^2}{T_{W0} - T_A}(T_W - T_A) = R_{W0} I_W^2 \tag{2.15}$$

Finally, we divide the equation by $R_{W0} I_W^2$ and multiplying by $T_{W0} - T_A$:

$$\frac{m_W c_W (T_{W0} - T_A)}{R_{W0} I_W^2} \frac{dT_W(t)}{dt} + (T_W(t) - T_A) = T_{W0} - T_A \tag{2.16}$$

Which is the same than:

$$\frac{m_W c_W (T_{W0} - T_A)}{R_{W0} I_W^2} \frac{dT_W(t)}{dt} + T_W(t) = T_{W0} \tag{2.17}$$

Remembering the differential equation of a simple RC circuit as the one of the Figure 2.1:

$$RC \frac{dV_0}{dt} + V_0 = V_i \tag{2.18}$$

which has a thermal inertia determined by $\tau = RC$. Hence if we consider $C_{th} = m_W c_W$ the *thermal capacitance* of the sensor and $R_{th} = \frac{\Delta T}{P_W} = \frac{(T_{W0} - T_A)}{R_{W0} I_W^2}$ its *thermal resistance*, then the time constant of the sensor is:

$$\tau_s = R_{th} C_{th} = \frac{m_W c_W (T_{W0} - T_A)}{R_{W0} I_W^2} \tag{2.19}$$

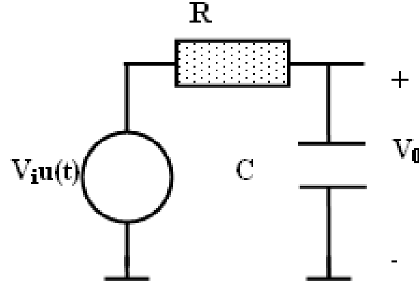

Figure 2.1: RC Circuit. Electrical equivalent or Thermal Circuit model of the sensor dynamics.

Moreover, R_{th} can be expressed in terms of the *Nusselt* number giving the fact that, according to equation 2.5 $\frac{T_W - T_A}{R_{W0} I_W^2} = \frac{1}{Nu\pi lk}$:

$$R_{th} = \frac{1}{Nu\pi lk} \tag{2.20}$$

In the other hand, the mass of the wire can be expressed in terms of its geometry and density. Since the volume of a wire is $V_W = \pi r^2 l = \pi \frac{d^2}{4} l$, then:

$$C_{th} = V_W \rho_W c_W = \pi \frac{d^2}{4} l \rho_W c_W \tag{2.21}$$

Therefore, the *time constant* (normally notated as M_W^{CC} instead of τ) of the sensor can be expressed independently from its geometry except its *characteristic length*:

$$\tau = M_W^{CC} = \frac{d^2}{4} \frac{\rho_W c_W}{kNu} \tag{2.22}$$

An important conclusion of this result is that high *thermal conductivities* and low *specific heat capacities* lead to faster responses. This result can be applied to any other first order thermal system.

Anemometer circuits

Three types of thermal anemometers are commonly used:

1. Constant Current Anemometer (CCA)
2. Constant Temperature Anemometer(CTA)
3. Constant Voltage Anemometer (CVA)

In a CCA the hot-wire anemometer is powered by a constant current I, the velocity of the flow is a function of the temperatures of the wire and the fluid:

$$U_f = f(T_W, T_f) = \left(\frac{\frac{I^2 R_0 (1+\chi(T_W - T_0))}{A_W (T_W - T_f)} - A}{B} \right)^2 \tag{2.23}$$

In this case, if the flow temperature is measured independently, the fluid velocity can be reduced to a function of the wire temperature T_W alone. In turn, the wire temperature is related to the measured wire resistance R_W. Therefore, the fluid velocity can be related to the wire resistance.

Now, the simple circuit configuration of a CCA can be seen in Figure 2.2. It is an open loop circuit which inverse the response of the sensor to get a suitable readout. There is voltage source which provides the current through the resistor R_B, of high resistance value that keeps the current in the sensor fairly constant despite changes in its resistance. An optional adjustable resistor in series with R_B can be placed for calibration purposes (i.e. fix current value).

The next stage is a high gain differential amplifier, which is frequently implemented with several stages. Response compensation is usually done using a simple RC circuit coupled to the amplifier. In order to adjust the circuit output a square-wave signal can be added to the heating current of the wire. The adjustment is correct when the square-wave signal is recovered at the output of the amplifier. Provided that it is an open loop configuration, this procedure may be repeated for any new operating condition which makes the technique quite unstable.

The thermal inertia of this circuit configuration is essentially the same of that of the sensor (See Eq. 2.22). This is once again a direct consequence of working in an open loop. Hence:

$$M_W^{CCA} = M_W^{CC} \tag{2.24}$$

On the other hand, in a CTA, the hot-wire anemometer is powered by an adjustable current to maintain a constant temperature, hence T_W and R_W are constants. The fluid velocity is a function of the input current and flow temperature:

$$v_f = f(I, T_f) = \left(\frac{\frac{I^2 R_W}{A_W (T_W - T_f)} - a}{b} \right)^2 \tag{2.25}$$

Furthermore, the temperature of the flow T_f can be measured so that the fluid is reduced to a function of input current only.

A basic circuit configuration of a CTA is shown on Figure 2.3. There is a feedback loop designed to hold the sensor resistance, and hence its temperature, constant. In fact, the bridge is balanced at a certain state which can be changed in case a reduction in the resistance of the sensor takes place, due to an increase in heat transfer which in turn causes a fall in temperature. Hence a positive error voltage is introduced at the output of the bridge. The differential amplifier therefore senses this unbalanced voltage from the Wheatstone bridge. After considerable amplification, the signal from the amplifier increases the bridge voltage and hence also the current through the sensor, so that the sensor is heated

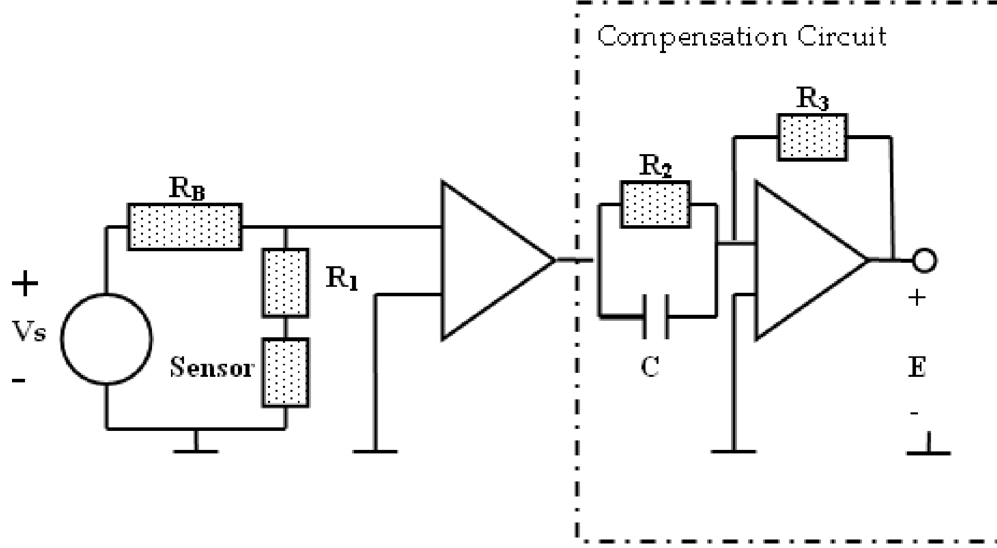

Figure 2.2: Basic configuration of a CCA. It includes a tensor divisor stage, a differential amplifier and a compensation circuit.

and the bridge balance is restored. If needed, a current booster could add the necessary current to cause this effect on the bridge. In this way the sensor temperature is kept essentially constant. Finally, the fluctuations in sensor current provide the anemometer output, voltage E, which is processed further.

The use of a closed-loop allows to dramatically reduce the thermal inertia of the anemometer. According to [15], the expression taking into account the resistances of the Wheatstone bridge R_1, R_2 and R_3:

$$M_W^{CTA} = \frac{M_W}{1 + 2Ga_W \frac{R_W}{R_W+R_1} \frac{R_2}{R_2+R_3}} \tag{2.26}$$

This equation shows that a symmetric bridge yields the smallest possible value for M_W^{CTA}, thus permitting the best frequency response.

Finally, CVA is a more recent technique which has been conceived and developed by [16] in late nineties. The sensor, either a wire or a film, is placed in the feedback loop of the operational amplifier. The voltage across it, $V_W = R_W I_W$ can be adjusted and measured, and once set it is independent of the hot-wire resistance R_W. Any change in wire resistance due to fluid flow produces a change of current in the wire, whose only path is through resistance R_2 (See Figure 2.4). The anemometer output V_s is closely related to the voltage drop in resistor R_2. The circuit parts involving R_{2a}, R_{2b}, and C with $R_2 = R_{2a} + R_{2b}$ permit a linear frequency increase of the CVA output and therefore the thermal lag compensation of the wire. The time constant T_C associated with this compensation is

$$T_C = \frac{R_{2a} R_{2b}}{R_2} C \tag{2.27}$$

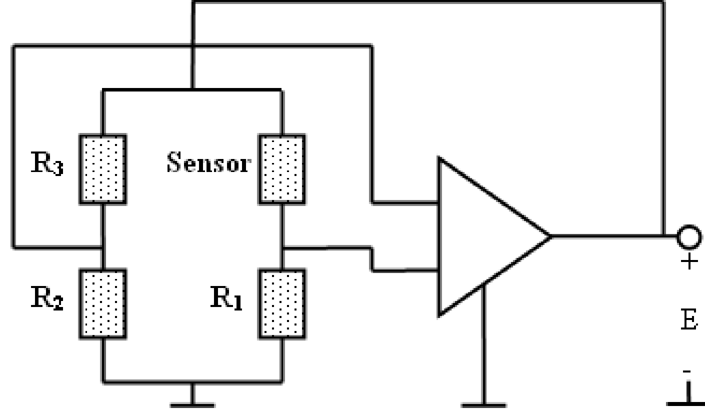

Figure 2.3: Basic configuration of a CTA. It includes a Wheatstone bridge and a differential amplifier

The Kirchoff analysis of the network leads to the following relation between the input voltage (V_1) and and the voltage within the sensor V_W:

$$V_W = V_1 \frac{R_F}{R_1} \tag{2.28}$$

Furthermore, from the same analysis, the transfer function $\frac{V_S}{V_W} = H(\omega)$ turns out to be:

$$\frac{V_S}{V_W} = 1 - \frac{R_2}{R_{2a}} + R_2 \left(\frac{1}{R_W} + \frac{1}{R_F} + \frac{1}{R_{2a}} \right) (1 + i\omega T_C) \tag{2.29}$$

In this case, time response is also reduced with respect the CCA operation mode but not as significantly as in the CTA configuration. Making a similar analysis as the one done before, the time constant can be deduced and it has the following value according to [16]:

$$M_W^{CV} = \frac{\rho_W c_W}{\chi R_0} \frac{1}{I_W^2} \frac{(R_W - R_A}{2R_W - R_A} = \frac{M_W^{CC}}{1 + 2a_W} \tag{2.30}$$

Materials

All the materials commonly used as a sensing devices in hot-wire anemometry are metallic elements (with a low electric resistance in the range $3 - 10\Omega$ at room temperature) which are easy to manipulate (See Figure 2.1). One of the most important parameters of these metals is its *temperature resistivity coefficient* χ which has to be controlled as long as the manufacturing process can influence the value. As a matter of fact, *chi* can vary significantly with the temperature which means that the temperature range in which the behavior of the material is linear has to be well known. Materials with good stability over a wide range are therefore preferable (e.g. platinum has a good linear response between -200°C and 850°C while other metals such as copper and nickel start modifying its pattern over 300°C [21]).

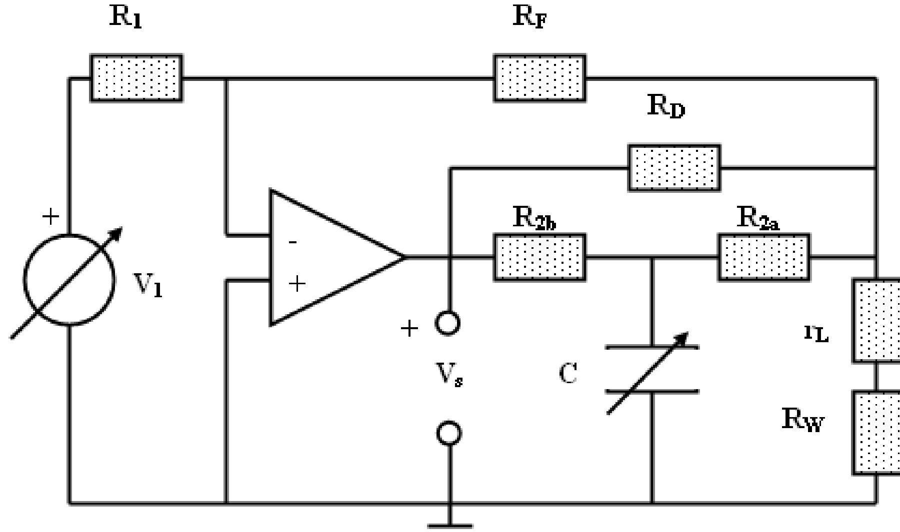

Figure 2.4: Basic configuration of a CVA. Conceived and developed recently by [16].

Indeed, platinum shows some advantages over other materials used in *Resistance Temperature Detectors* (RTD) which makes it one of the most suitable materials for this technique except for its cost. These can be summarized as follows:

1. Higher long term stability.

2. Higher accuracy.

3. Bigger linearity range.

Recently, micromachining technology has allowed the use of other materials such as Polysilicon with large electric resistances around $0.5 - 5k\Omega$ (See Table 2.2). Although only a few laboratories are currently equipped to make them, mass production is possible as a single silicon wafer can encompass a large number of sensors. This technology allows further reduction of the wire size therefore decreasing power consumption and thermal interference to the flow, better device sensitivity and spatial resolution and increase frequency response by at least one order of magnitude over conventional hot-wire anemometers. Doping of the polysilicon allow a good control of its parameters such as the *temperature coefficient of resistance* which can be set from $-1\%/^{o}C$ at doping concentrations of 10^{18} to $+0.2\%/^{o}C$. Optimization of the structural geometry and the material properties has resulted in anemometers with time constant of $2\mu s$ ($f_s = 500kHz$) working in CTA mode, being the current record for thermal anemometers [19].

With respect to the sensor dimensions, large aspect ratios are preferred (for instance, this ratio is defined in wires as $\frac{l}{d}$, where l is the length and d the diameter of the wire. Thus, when $\frac{l}{d} > 300$, the wire can be cooled by the normal component of the fluid velocity, with negligible heat transfer to its supports (buoyancy effect). In fact, according to [17]

Material	Resistivity (Ωm)	Temperature coefficient of resistivity χ ($\frac{1}{K}$)	Density ρ ($\frac{kg}{m^3}$)	Specific heat c ($\frac{J}{kgK}$)	Thermal conductivity k ($\frac{W}{mK}$)
Copper	1.6×10^{-8}	$+4.0 \times 10^{-3}$	8900	385	400
Nickel	7.0×10^{-8}	$+6.0 \times 10^{-3}$	8900	438	90
Platinum	1.1×10^{-7}	$+3.9 \times 10^{-3}$	21500	130	70
Pt/10%Rh	1.9×10^{-7}	$+1.7 \times 10^{-3}$	19900	150	40
Silver	1.6×10^{-8}	$+3.8 \times 10^{-3}$	10500	235	428
Tungsten	6.0×10^{-8}	$+4.5 \times 10^{-3}$	19300	140	170
Silicon	2.3×10^{3}	-7.5×10^{-2}	2330	705	148

Table 2.1: Table showing properties of metal materials commonly used as anemometers, extracted from [18]

Material	Resistivity (Ωm)	Temperature coefficient of resistivity χ ($\frac{1}{K}$)
High P doping	5×10^{-5}	$+1.0 \times 10^{-3}$
Low P doping	5×10^{-5}	-2.5×10^{-3}
B doping 2×10^{-5}	$+8.5 \times 10^{-4}$	
B doping $2 \times 10^{16}/cm2$	5×10^{-5}	$+8.0 \times 10^{-4}$

Table 2.2: Table showing properties of polysilicon materials used used in micromachining to work as anemometers [18]

there is a criterion that permits to ensure that forced convection prevails for a cross-flow:

$$Re > Gr^{1/3} \tag{2.31}$$

where Re is the *Reynolds* number (See Equation 2.6) and Gr is the *Grashoff* number:

$$Gr = g\beta(T_W - T_A)d^3 \left(\frac{\rho}{\mu}\right)^2 \tag{2.32}$$

where g is the gravitational acceleration, β the *thermal coefficient of expansion at constant pressure*, ρ the density of the fluid and mu the *Newtonian coefficient of dynamic viscosity.*

Protective Coating

In the field of anemometry research the topic of protection layers coated over the sensor material is certainly not a central topic. However it is of particular interest in this work because it shares many characteristics with the interface layer we are willing to design.

According to [13], the coating of hot-wire probes was firstly tried to overtake the problem of electrolysis which makes an unprotected sensor useless for measurements in a conducting medium such as water. Technological difficulties arose because it was not easy

to make thin coatings impervious to water, not too thick to make the probe very insensitive to velocity fluctuations. Hence ,the development of the hot-film probe with thin quartz coatings (which corresponds to SiO_2, one of the alternatives studied in this work) of $1 - 2\mu m$ solved the electrolysis problem. In this way in [13] it is stated that "The thin protective layer has a negligible effect on the frequency response, except for frequencies above about 50kHz.". However, [20] mentions that "in practice, the bandwidth is determined by the *damping effect* of the backing substrate, the protecting quartz coating and the flow boundary layer".

On top of that, according to [20] nowadays protective coatings are used not only for liquid applications but for protection against wear and oxidization in gas applications. In this case, thicknesses of around $500nm$ are used.

Although coatings of quartz are the most common protective solutions, [13] also reports the use of alumina (aluminum oxide, Al_2O_3) coatings to prevent the sensor film from being eroded when exposed to dirty gas flows.

In short, the use of a protective coating causes a damping effect in the interaction of the sensor material with the fluid, but this effect is negligible at frequencies below 50kHz.

In this particular design proposed for the MetNet mission however, it will be shown in the next section that this isolation layer becomes more important and why this is so. Some of the reasons are:

1. The surface of the sensing area is wider than that of the platinum film sputtered on it.

2. The substrate of the sensor will be meant to isolate the sensor from the rest of the equipment so that heat conduction through the sensor surface will have to be done mostly by means of this layer.

3. It might exists a resistance with the only purpose of heating the contact area apart from the sensing resistance. To this end, heat gradients should be controlled and minimized.

2.2 Fabrication Technology

In this section the fabrication technique which makes possible the fabrication of the film probe and its isolating layer, which has been explained in the previous section, is presented. *Sputter Deposition* technique has been chosen due to the following reasons:

1. It is possible to achieve extremely thin depositions (less than $100nm$).

2. They can be made regardless the material and surface geometry.

3. All the process can be carried out at room temperature.

4. The availability of the technology in our clean room and the significative previous experience with this technique in sensors design and other fields of research.

Accordingly, now sputter deposition principles are presented as well as its different operation modes, its capabilities and limitations.

2.2.1 Sputter Deposition

Sputter deposition is a *physical vapor deposition* (PVD) technique of depositing thin films ejecting material from a source which then deposits onto a substrate.

In the sputter system an inert gas, such as argon, is fed into the sputtering chamber at low pressure. As soon as this is done, a voltage is applied across two electrodes and a plasma is created. The plasma contains neutral argon atoms, and roughly equal numbers of positive ions and free electrons, and is a conducting medium. In one of the two electrodes, a negative DC bias voltage is applied, which actually is the source material to be deposited, for instance a plate of Al, C, Si, etc. This electrode becomes the cathode and is called the *target*. The opposite electrode is a grounded metal plate where the wafer is subjected, and becomes the anode.

The positive ions in the plasma are accelerated to the negatively biased target, which can be several hundred to several thousand volts negative relative to the plasma. These energetic ions strike the target and dislodge, or sputter, the target atoms. These atoms are then free to travel through the plasma as a vapor and strike the surface of the wafers, where they condense and form the deposited film.

RF Sputter Deposition

When only a constant negative voltage is applied to the cathode the technique is called *DC Sputter Deposition*. This technique though, can be applied just in case the source material is conductive. Therefore Al, W, Ti, silicides, and other metals can be sputtered this way. Hence, to deposit nonconductors such as oxides, nitrides, and lightly doped silicon a biased oscillatory voltage must be applied to the cathode and then the technique is called *RF Sputter Deposition*. Since we will mostly focus on insulators (See Section 3.3) in this work, *RF Sputter* deposition will be applied.

Reactive RF Sputter Deposition

In addition, there is a way in which compounds can be sputter deposited. A reactive gas is introduced into the sputtering chamber in addition to the Ar plasma, and the compound is formed by the elements of that gas combining with the sputtered material. For instance, nitrogen or oxygen are common reactive gases used in this technique. The plasma can therefore furnish energy to the N_2 or O_2 gas to allow it to dissociate into single atoms, which then can easily react with the target element. In this project compounds such as AlN, CN_x, SiO_2 have been created by sputtering using this technique, commonly known as *Reactive Sputter Deposition*.

Magnetron Sputter Deposition

In both conventional DC and RF sputtering, the efficiency of ionization from energetic collisions between the electrons and gas atoms is rather low. Most electrons lose their energy in non-ionizing collisions or are collected by the anode, and only a small percentage of them take part in ionization processes with the Ar atoms. In RF plasmas electrons gain energy directly from the oscillating RF fields, increasing the ionization efficiency somewhat. Nevertheless, the overall ionization efficiency is still fairly slow. As a result, the deposition rates are usually rather low. Few Ar atoms are converted to positive ions and few positive ions strike the target.

In the technique known as magnetron sputtering, magnets are used to increase the percentage of electrons that take part in ionization events, and the ionization efficiency is increased significantly. A magnetic field is applied at right angles to the electric field, usually by placing large rectangular magnets behind the target. This traps the electrons near the target surface, and causes them to move in a spiral motion until they collide with an Ar atom. The ionization and sputtering efficiencies are increased significantly, and deposition rates of up from to 10 to 100 times faster than without the magnetron configuration can be achieved. Unintentional wafer heating is also significantly reduced, because the dense plasma is confined to near the target and the ion loss to the wafers is less. Besides, a lower Ar pressure can be utilized since the ionization efficiency is so much larger. This can lead to better film quality given the fact that less argon will be incorporated in the film. At these higher ion currents, cooling of the target can be a problem for RF systems which have insulating targets.

Chapter 3

Sensor development

3.1 Previous developments

Rarely happens that a design meant to an important mission as *MetNet* is started from scratch. Normally long experience is required due to the complexity of the processes involved. Not only a deep theoretical understanding of the physical phenomena is important, but also the technological means and the ability to manage them properly are key items. In this way, it would be impossible to succeed without the long experience gained by many years of collaboration in similar and related projects. An illustrative example of this fact is the mere existence and conservation of a hundred percent operational clean room which makes possible the research and fabrication of devices such as this.

3.1.1 REMS

The design of the present wind sensor is based on the knowledge and experience gathered from the previous hot film anemometer developed in the Department of Electronics of the UPC which will be included in the *Rover Environment Monitoring Station* (REMS). REMS is a part of the *Mars Science Laboratory* (MSL) and it consists of a set of equipment to provide measurements of wind speed and direction, ground and air temperature, pressure, humidity and UV radiation. The launch is scheduled for the fall of 2011 after being delayed. Problems arisen in REMS wind sensor design have provided *know how* which has been applied to the subsequent MetNet project using a more elaborate concept. It is therefore important to explain here how the REMS wind sensor works as well as its strengths and weaknesses.

In REMS wind speed and direction is derived based on information provided by three two-dimensional wind sensors located in two booms of the REMS. In each boom, the three sensors are located 120° apart around the boom axis. Each of them record local speed and direction in the plane of the sensor. Hence a convolution of the 12 data points is enough to determine wind speed, pitch and yaw angle of each boom relative to the flow direction.

According to results obtained in Mars-like environment simulations it determines horizontal wind speed with $1m/s$ accuracy and $0.5m/s$ of sensitivity between 0 and $70m/s$

of range. The directional accuracy is around 10º. The same accuracy and resolution is expected to have in the vertical direction, but with a range of 0 to $10m/s$.

The design approach followed in the REMS wind sensor has been the application of a variation of the standard first-order sigma-delta topology ($\Sigma\Delta$) theory to sensors. In addition, the operation mode is a variation of the *Constant Temperature Anemometer* (CTA) described in Section 2.1 called *Constant Temperature Difference Mode* (CTD). Here the temperature of the sensor is kept at a constant difference of the temperature of the fluid, which is assumed to vary slowly. In fact, *Thermal sigma-delta modulation* operating as a control circuit turns out to be an excellent tool to implement this operation mode.

The principle of measurement is the following: There are four dice, a complete CTA each containing two resistors:

1. A temperature sensing element (sensor).
2. An additional heater that controls the die temperature.

They produce two dimensional sensitivity to the wind in the sensor plane. In addition, there is a reference point. The temperature of each of the four dice and that of the reference point are measured and compared by the sigma-delta control circuit which heats every one. Hence the four thermal energy convected to the ambient can be inferred from it. Their relative difference is a function of the wind incidence angle at that plane which can be deduced as well.

The resistor material chosen was platinum due to its good response and linearity at low temperatures (between -200 and 480ºC), corresponding to those found in Mars (from -143ºC to 20ºC). Indeed, its reliability is widely proven since is the basis of most commercial temperature sensors today. Furthermore, contrary to the common scenario in earth or with anemometry of liquids, the low pressure of the atmosphere required enough contact area to provide enough interaction with the sensor. The *Knudsen* number, which is defined as

$$\frac{\lambda}{l} \tag{3.1}$$

where λ is the mean free path of the atmosphere molecules and l is the characteristic length of the device, is therefore larger than in an equivalent system located in the Earth. This impose a minimum quantity in the size of the device so that the medium can be considered continuum. In order to increase the contact surface the hot film probe had to be spread through the surface of a chip which interacts as a whole with the surrounding air.

The chip is fabricated using a silicon bulk material which is later thermally oxidized (SiO_2) to provide thermal conduction through the die and electrical isolation between the resistors. Hence the problem studied in this work was solved in REMS using a $90nm$ thick SiO_2 substrate. This option is studied and evaluated in further sections of the report.

Special care was taken of the thermal losses from the die to the rest of the sensor structure. In Mars atmosphere, due to its low pressure, the convective energy transfer is much smaller compared to that under Earth conditions. That is why losses by conduction become much more significant in proportion. Thus improving substrate isolation was a

key point in the design of REMS wind sensor. An inverted table made of Pyrex was the solution adopted. Each of the four dice were held by its corresponding support. However, results obtained showed that thermal losses still persisted and that isolation was a weak point of the design. Although the final functionality is satisfactory enough, further research was needed in this field.

Finally, connectivity between the electronic circuit (substrate) and the sensor (die) pads was made using wires. This option is also suboptimal from the point of view of reliability. Wires can be broken easily and require human direct intervention along the fabrication process since each bonding has to be checked which can affect other parts of the electronics. This could be critical in this kind of mission where resistance to vibrations, shocks and long term degradation is a must. However the general concept of the sensor obliged to adopt this solution.

3.2 Prototype

The conceptual idea of the ongoing design of the MetNet wind sensor is presented in this section. As explained in the previous section the starting point has been the successfully designed REMS wind sensor. For instance, the general idea of a hot film anemometer controlled by a closed loop architecture is to be maintained. In this way, the thermal sigma-delta converter which provides the feedback as well as a direct digital readout of the magnitude measured is not changed.

Hence the novel idea of the MetNet wind sensor is the use of a solid sphere as can be seen in Figure 3.1. Using this shape will allow to increase significantly the contact area with the environment as well as the robustness of the structure. In this case, the sensor must be able to resist a shock force of 500G (See Section 1.1) which means that a strong structure is needed. This sphere is made from a thermal isolator in order to decrease heat losses to the rest of the structure and within the different sectors. The sensor probe itself is made from Platinum which is sputtered over the surface. However, in order to increase the adherence between the substrate and the platinum a thin layer of Titanium is sputtered before. It is divided in several sectors electrically isolated between them. To do this, a separation between sectors is created with a laser that cuts the platinum and opens and empty space between them. Each one contains the sensing resistor circuit which patterns are also created by means of a cutting laser.

Furthermore, it is expected that no wires will be needed since metal pads will be also sputtered over the surface through the sphere structure till the corresponding electronics.

Sphere dimensions (i.e. diameter) are chosen so that flow is laminar. *Reynolds* number sets the limit between turbulent flow (large number) and laminar flow (small number). This limit is reached at $Re = 2 \times 10^5$. If Re definition is given by the following expression:

$$Re = \frac{\rho D U}{\mu} \tag{3.2}$$

where ρ is the density of Martian air, μ its viscosity, D the diameter of the sphere and U the wind speed. According to this, if Re is set at some constant value and being ρ and μ

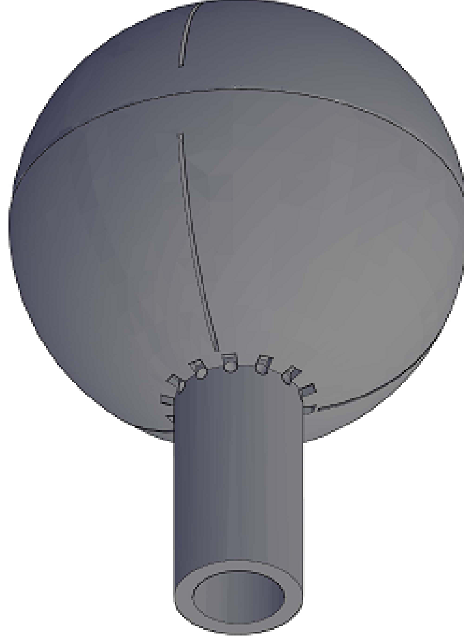

Figure 3.1: Spheric sensor with several sections in both hemispheres. 3D image created with AUTOCAD. Published with the permission of Samir Kassar.

intrinsic constants of the environment, relation between D and U is given by:

$$U = \frac{K}{D} \tag{3.3}$$

which sets a trade off between the minimum diameter of the sphere and the maximum wind speed that can be measured for a given constant $K = \frac{Re\mu}{\rho}$. The bigger is K (bigger Reynolds number), the bigger can be the sphere dimensions for the same wind velocity maximum. In the other hand the bigger is the *Reynolds* number, the closer is the flow to a turbulent one. In fact, if a steady flow requires $Re < 270$, a steady and axisymmetric flow requires $Re < 210$, both characteristics being desirable in order to avoid noisy measurements (turbulences) in the sectors opposed to the wind flow. For instance, to achieve $Re < 270$, diameter should be smaller than $15mm$ so that $10m/s$ wind velocities can be measured. If speeds up to $35m/s$ are to be measured, then a diameter below $5mm$ is required. Very small diameters could lead to fabrication problems difficult to solve such as low resistance of the platinum, too thin metal pads, etc. speeds up to $35m/s$ are to be measured, then a diameter below $5mm$ is required. Very small diameters could lead to fabrication problems difficult to solve such as low resistance of the platinum, too thin metal pads, etc.

Furthermore, convected power by the sphere to the air is related to the *Nusselt* number which in turn, increases with the *Reynolds* number. Hence *Reynolds* number should not be as small as possible but bigger enough to maximize convected power without compromising flow desired characteristics.

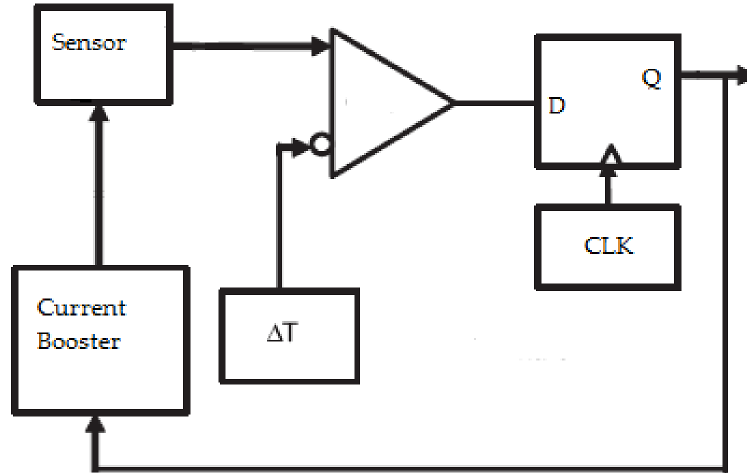

Figure 3.2: Sigma-delta converter in the particular configuration suggested for the MetNet sensor design.

The control circuit will be based on the *Constant Temperature Difference* operation mode. To do so, as mentioned before, an electro-thermal sigma-delta modulator will be used. Sigma-delta modulators are a singular type of A/D converters. They can be seen as a 1-bit A/D where the bit value (high or low) indicates an increase or a decrease in the input. It therefore supposes that variations are smooth at the sampling rate. This means that oversampling is needed, that is, the bandwidth of the input signal has to be much lower than that of the converter so that variations in the input signal can be followed by the converter with increases of one step each clock. Due to this reason, it has been traditionally used for low and medium frequency signals like audio, etc. In this sense, a sigma-delta converter can be interpreted as a digital *voltage-controlled oscillator* (VCO) where the "frequency", that is, the density of pulses is proportional to the level of the input. Their main advantage is its robustness in front of imperfections of the components which allows the use of cheap electronics. There is a huge amount of different circuit topologies of sigma-delta converters, but the simplest one and maybe the most used in sensors and actuators is that of first-order. The block diagram of the Figure 3.2 shows how the loop works.

First, an offset current namely I_{off} is injected by the *current booster* heating the sensor to keep its temperature at a minimum level. In steady conditions, this temperature is compared with the reference temperature (which is related in turn with the ambient temperature), if the sensor temperature is lower, then the comparator place a high voltage level in the *D biestable* connected to its output. Actually, temperature is indirectly measured by measuring resistance value which in turn is directly related with the voltage given a constant current. When next clock happens, the state Q of the biestable changes into "1" which is set at its output as well. Hence this signal reaches the *current booster* which injects then a high level current namely I_{on} further heating the sensor until its temperature

reaches the reference one. When this happens, the comparator output will change to a low level, and the next clock will change the current of the power pulser to I_{off} which in turn will decrease the sensor temperature again. Thus, in steady conditions the sensor temperature tend to be the reference temperature which is the sum of the ambient temperature and a preset increment $T_A + \Delta T$.

However, an incoming flow of air at a certain velocity that reaches sensor surface will cause an additional decrease of its temperature with respect that of steady conditions. In order to maintain the temperature of reference, the circuit will increase the probability of the state "1" with respect the state "0" compared to that proportion in an isolated environment. Thus if a low pass filter is placed at the output of the circuit, its level will be proportional to that probability which is turn dependent on the velocity of incoming flow. However an other option is to take advantage of the digital nature of the readout to place a digital counter which value observed after a certain period of time will be proportional to that speed as well.

Ideally, the temperature of the sensor would be always constant (if the ambient temperature does not change at all) and therefore no response analysis would be needed. Nevertheless, intrinsic characteristics of the feedback circuit such as the clock frequency, or the limited value of I_{on} sets some limitation in the capacity of the circuit to maintain the sensor temperature completely constant. Furthermore, not all the surface of a particular sector of the sphere will be affected exactly in the same way by an incoming flow since the incidence angle of it will be different depending on the sphere position. Indeed, assuming that heating in the platinum happens simultaneously in all its parts (which is relatively true as a first approximation) it is not assumable that all the surface of the sector, that is, all the interaction area is heated simultaneously. Hence temperature gradients are likely to appear which limits the dynamic response of the sensor and its ability to detect incoming with an homogeneous sensitivity incoming flows from different directions.

In last section, it was explained that REMS used an additional "heating resistor" which was spread along all the surface while the real sensor probe was heated by its own current. This resistor, helped by the good conductive behavior of the silicon dioxide substrate allowed decreasing gradients in the die surface. However, since the platinum itself is in fact part of the contact surface, gradients are still significantly and therefore the effective area where thermal convection happens is much lower than the physical area of the die.

The solution proposed in MetNet, and the main field of study of this work, is to provide a coating which is deposited over all the sector surface in order to help increasing the thermal conductivity within the sector area as well as providing a more thermally homogeneous contact surface with the air flow. Doing this, the platinum will not be in direct contact with the air anymore, but the coated material which is expected to spread by conduction its thermal energy much more efficiently and eventually convect it to the surrounding air with a much larger effective area. The cost of doing so is that this coating could certainly affect the time response at very high frequencies compared to the direct convection of the platinum as explained in Section 2.1 where traditional quartz coating was reviewed. However, this "damping effect" is far from being critical at this point where temperature gradients restrain its time response much more as well as limit the direction

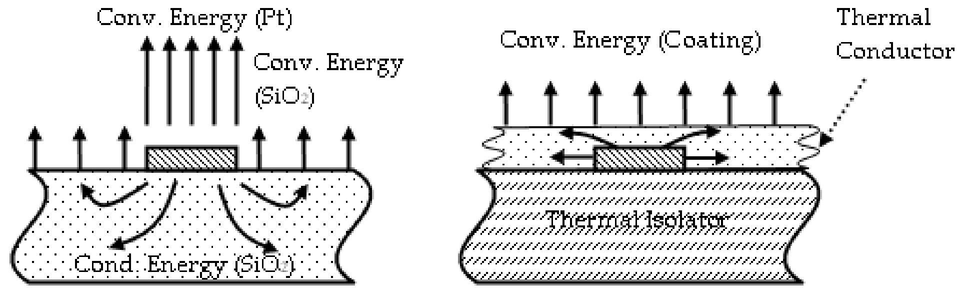

Figure 3.3: At the left, the heat flow of the REMS wind sensor. The platinum transfers the most important part of the total thermal energy convected to the air. The substrate (SiO_2) conducts part of thermal energy of the platinum (Pt) through its mass and a small proportion is convected in turn at its surface. The rest is stored at its high thermal mass or conducted to other parts of the structure. At the right, the heat flow of the MetNet wind sensor. The platinum transfers all its thermal energy by conduction, mostly to the *thermal conductor* and a small part to the *thermal isolator*. Also small energy is stored in the thermal mass of the coating since its really thin (100-200nm) compared to the REMS substrate. Therefore most part of the energy is effectively convected to the air by the coating after being spread uniformly through all its surface.

sensitivity and its homogeneous accuracy.

Furthermore, in REMS the multiple uses of the substrate material had a trade off between its thermal isolation which was a benefit in order to decrease heat losses and its thermal conductivity which helped decreasing temperature gradients. In addition, the substrate was expected to provide enough robustness which limited its minimum mass and hence its *thermal mass*. In MetNet is proposed to split this contradictory functions with this additional coating. In one hand, the substrate can be now a good thermal isolator minimizing heat losses conducted to the sensor structure, it can be also robust enough to resist heavy shock forces. In the other hand, the coating material can be selected *ad hoc* to provide the best thermal conduction through the contact surface and significantly decreasing the effective thermal mass to be heated.

A comparison of the two cases is shown in Figure 3.3. In the left image conduction in the substrate happens in all direction uniformly heating the large thermal mass of the device. Conduction to the substrate is also less than that to the coating shown in the right image since part of the thermal energy is directly convected to the air and only one side of the platinum section is in contact with the substrate. In right image however three sides of the section are in direct contact with the coating and conduction to the substrate is difficulted by its thermal isolation. Thermal losses are therefore significantly reduced. Conducted energy to the coating is then rapidly spread through its low thermal mass due to its high thermal conductivity before convection to the air even starts. Finally, the thermal energy is convected to the air in a much more homogeneous way since only the thermal conductive coating is in direct contact with it. This virtually expands the effective area of

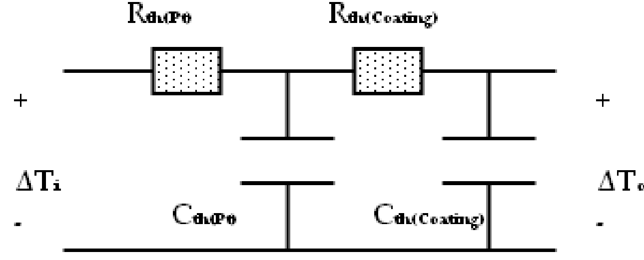

Figure 3.4: Second order thermal low pass filter modeling heat flow effect of coating over the sensor.

interaction where a constant temperature of the sensor can be assumed and hence enhances the *Knudsen* number ensuring a continuum behavior of the low pressure atmosphere.

The "damping effect" caused by the coating can be easily modeled by a *thermal low pass filter* which is coupled to the sensor's own structural thermal filter studied in Section 2.1 so that its time response is that of the linear network formed by the RC chain (See Figure 3.4). If transfer function of a RC network is:

$$H_{RC}(s) = \frac{1}{1+\tau s} \tag{3.4}$$

being τ the response time of the circuit ($\tau = R_{th}C_{th}$). Then the transfer function of the RC chain becomes the multiplication:

$$H(s) = H_{Pt}(s) \times H_{coating}(s) = \frac{1}{1+\tau_{Pt}s}\frac{1}{1+\tau_{coating}s} = \frac{\frac{1}{\tau_{Pt}\tau_{coating}}}{s^2 + s\left(\frac{\tau_{Pt}+\tau_{coating}}{\tau_{Pt}\tau_{coating}}\right) + \frac{1}{\tau_{Pt}\tau_{coating}}} \tag{3.5}$$

which, according to the general form of a second order transfer function:

$$H(s) = \frac{k\omega^2}{s^2 + 2\xi\omega s + \omega^2} \tag{3.6}$$

we have:

$$\begin{aligned} k &= 1 \\ \omega^2 &= \frac{1}{\tau_{Pt}\tau_{coating}} \\ \xi &= \frac{\tau_{Pt}+\tau_{coating}}{2\sqrt{\tau_{Pt}\tau_{coating}}} \end{aligned} \tag{3.7}$$

It is interesting to note that this network leads always to an *overdamped* or *critically damped* response ($\xi \geq 1$) because

$$\frac{\tau_{Pt}+\tau_{coating}}{2} \geq \sqrt{\tau_{Pt}\tau_{coating}} \tag{3.8}$$

that is, the *arithmetic mean* is always equal or greater than the *geometric mean* which means that no overshoot will not take place in any case. In the particular case where overdamping happens, both poles of the circuit are real and frequency response is governed by the one of lowest cutoff frequency, that is, *time response* of the circuit will be:

$$\tau \approx \frac{1}{(\xi - \sqrt{\xi^2 - 1})\omega} = \frac{1}{(\frac{\tau_{Pt}+\tau_{coating}}{2\sqrt{\tau_{Pt}\tau_{coating}}} - \sqrt{\left(\frac{\tau_{Pt}+\tau_{coating}}{2\sqrt{\tau_{Pt}\tau_{coating}}}\right)^2} - 1)\omega} \tag{3.9}$$

simplifying the expression forcing $\xi \geq 1$ it becomes:

$$\tau \approx \frac{2\tau_{Pt}\tau_{coating}}{\tau_{Pt} + \tau_{coating} - |\tau_{Pt} - \tau_{coating}|} \tag{3.10}$$

Hence if $\tau_{Pt} > \tau_{coating}$ then $\tau \approx \tau_{Pt}$, but if $\tau_{Pt} < \tau_{coating}$ then $\tau \approx \tau_{coating}$.

A more accurate approximation of the *rise time* is achieved in [25]. As a result of the *central limit theorem* applied to a low pass filter of n cascaded stages with no overshoot, its rise time t_{rn} is of the form:

$$t_{rn} = \sqrt{t_{r1}^2 + t_{r2}^2 + ... + t_{rn}^2} \tag{3.11}$$

where t_{r1} is the rise time of the first stage, t_{r2} the rise time of the second stage and so forth. Although this is a limit result when n tends to infinite, reported observations show that the approximation is very good, usually within 10 percent, for values of n as small as 2.

In short, it is concluded that in any case $\tau_{coating}$ should be as small as possible being the ideal case $\tau_{Pt} >> \tau_{coating}$ when no perceptible perturbation in time response is introduced by the coating at all.

If now, the coating is modeled as a plate of area A_c, and thickness L_c and thermal conductivity k_c, then its thermal resistance is defined as:

$$R_{th} = \frac{L_c}{k_c A_c} \tag{3.12}$$

and its thermal capacitance:

$$C_{th} = V_c \rho_c c_c = A_c L_c \rho_c c_c \tag{3.13}$$

where V_c is the volume, ρ_c the density and c_c the specific thermal capacitance. Finally $\tau_{coating}$ will be:

$$\tau_{coating} = R_{th} C_{th} = \frac{L_c}{k_c A_c} A_c L_c \rho_c c_c = \frac{L_c^2 \rho_c c_c}{k_c} \tag{3.14}$$

Therefore, low specific thermal capacitance, low density and high thermal conductivity will be desirable features of the material chosen. This three parameters can be merged in a single one called *thermal diffusivity* $\alpha(cm^2/s)$ which should be as large as possible. It is defined:

$$\alpha_c = \frac{k_c}{\rho_c c_c} \tag{3.15}$$

In next section various materials are presented according to this and other properties.

3.3 Isolation materials

In this section the different compounds studied in this work are presented. These are: Silicon Oxide (SiO_2), Aluminum Nitride (AlN) and Carbon Nitride ($\beta - C_3N_4$). They have been selected to match the needs explained in the previous section but also taking into account the fabrication process and the availability of the necessary targets to fabricate and deposit them. Tin oxide (SnO_2) was considered in the first stages of the research because there was previous experience with this material. Some depositions were made, but its electrical conductivity was too high to work as a insulator. Later on, bibliographic research showed that electrical resistivity of this material is in the scale of $10^{-4}\Omega cm$ [26] and therefore this option was abandoned.

Some *a priori* good candidates such as Beryllium Oxide (BeO) or Boron Nitride (BN) had to be dropped out because needed targets were not at the clean room. In some cases such as Silicon Carbide (SiC)the fabrication was not possible with the available means. Others because it seemed to be worse options and it would be very time consuming to carry out an exhaustive experimentation. This was the case with Silicon Nitride (Si_3N_4) or Aluminum Oxide (Al_2O_3).

Although properties of Silicon Oxide (SiO_2) are much worse in terms of thermal conductivity than the others, its previous use in REMS, its perfect behavior as electrical insulator and the purpose of compare the other candidates with it, it has been chosen as reference candidate. AlN is therefore the *a priori* most suitable candidate because is well recognized as an insulator with good thermal properties. Its thermal conductivity is only beaten by that of the toxic *Beryllia*. Finally, Carbon nitride was chosen as a completely different option. It is a very new material which properties are barely known. However, its properties are expected to be very similar to those of diamond. If diamond could be deposited by sputtering, it would be the best option both as an electrical insulator and a thermal conductor, that is why carbon nitride gained attention and rose reasonable hopes of behaving well.

In table 3.1, relevant properties of the materials mentioned above plus the ones actually studied are listed.

3.3.1 Silicon Oxide

Silicon Oxide (SiO_2) is commonly named *Silica* and it is one of the most abundant oxide materials in earth and it occurs in nature as sandstone, silica sand or quartzite. Whenever silicon Si is exposed to air a small film of silicon dioxide (native oxide) with a thickness of approximately $1nm$ is formed on the surface. It is the source material for the production of silicate glasses such as window glass, drinking glass and bottled leverages. Most of optical fibers are also made from silica. Besides it is a primary raw material for ceramics. It can exist in a variety of crystalline forms such as quartz, tridymite and cristobalite within others.

Silica is manufactured in several forms including glass, crystal, gel, aerogel, fumed silica, and colloidal silica.

Material	Th. Diffusivity (cm^2/s)	Resist. (Ωcm)
SiO_2	0.0082 [27]	$10^{12} - 10^{16}$
AlN	0.46-0.52 [28]	10^{16} [29]
$\beta - C_3N_4$	0.007 [30]	$10^3 - 10^7$ [44]
Al_2O_3	0.077 [32]	$> 10^{14}$
Si_3N_4	0.257 [32]	10^{12} [33]
SiC	0.334 [32]	$10^2 - 10^6$
BN	0.32 [34]	$> 10^{14}$
BeO	0.102-0.217 [35]	$10^{11} - 10^{12}$ [36]

Table 3.1: Materials mentioned in the text. Their thermal diffusivity and electrical resistivity are listed. Data is extracted from references given.

High purity grade of silica is called *fused silica* and is used in the electronics industry where its good dielectric and insulating properties are exploited. It is grown as thin film of silica on silicon wafers via *thermal oxidation* which creates high quality interfaces between silicon and silicon dioxide. Most of the times, the Si atom shows a tetrahedral coordination, with four oxygen (O) atoms surrounding a central Si atom. However two of them are shared with others, yielding the the net chemical formula SiO_2. Its electrical and thermal properties can vary widely depending on its crystalline structure. Essentially all deposited (CVD and PVD) and thermally grown oxides in semiconductor are amorphous ($a - SiO_2$) which leads to worse properties than those of more perfect structures.

Fabrication

Silicon Oxide has been the first material investigated in this work. It has been deposited on various surfaces (in the case of silicon wafers, their native oxide was previously removed with HF acid 5% attack) by sputtering with a Silicon (Si) target in an atmosphere of Argon ($5sccm$) and Oxygen ($10sccm$) at a process pressure at the vacuum chamber of $5 \times 10^{-3} mbar$ and room temperature. Plasma easily formed using this configuration with a power of $200W$. In all cases, before the processes began a base pressure of around 1×10^{-5} was achieved inside the vaccum chamber of the sputtering which took around 2 hours depending on muliple conditions.

3.3.2 Aluminum Nitride

As mentioned above, SiO_2 film is one of the most common insulating materials in microelectronics field. However, application of SiO_2 insulating layer in integrated circuits is limited by the self heating effect which degrades operation and reduce device lifetime, caused by its poor thermal conductivity ($\approx 1.3W/mK$). AlN has been therefore investigated recently as possible alternative with a thermal conductivity about 100 times than that of SiO_2 ($\approx 140W/mK$) [37].

Aluminum Nitride (AlN) is a relatively new material in the technical ceramics family. Although it was first discovered in 1862 by F. Briegler and A. Geuther and the first synthesis was realized by J.W. Mallets in 1877, within the last 25 years it has been developed into a commercially viable product with controlled and reproducible properties.

It has a hexagonal crystal structure called *wurtzite* and is a covalent bonded material. The material is stable to very high temperatures in inert atmospheres. In air, surface oxidation occurs above 700°C. Between 700°C and 1370°C only a thin layer of oxidation forms though which protects the rest of the material. Above this temperature bulk oxidation occurs. Aluminum nitride is stable in hydrogen (H)and carbon dioxide (CO_2) at low temperatures (under 1000°C). It has good dielectric properties as well as high thermal conductivity. Its thermal expansion coefficient is relatively low, close to that of Silicon.

Contrary to expectations in the early 1990s the use of AlN ceramics has been restricted to a few products only. AlN has always been compared with *alumina* (Al_2O_3), the typical ceramic package material. Although the price of AlN has decreased over the past few years, advantages of material characteristics do not compensate for the cost differential. There is only a small number of companies which can produce AlN in large volumes and most vendors of powders, substrates and packages are headquartered in Japan.

Within its common application it is used as substrate for electronic packages, heat sinks, power transistor bases, microwave device packages, material processing kiln furniture, semiconductor processing chamber fixtures and insulators and molten metal handling components. It is special interesting in the electronics area where heat removal is important. In comparison to other electrically insulating ceramic materials only *Beryllium Oxide* (BeO) offer higher thermal conductivities. However, it has been banned by numerous manufacturers because of its toxicity. Hence AlN is a good non-toxic alternative to Beryllia (BeO) for most applications. Besides, its piezoelectric properties (piezoelectric coupling factor) are promising for a wide range of applications in optics, mechanics and electronics [38]. AlN based devices can be used in the deep ultraviolet wavelength due to its wide direct band gap ($Eg = 6.2eV$), high refractive index and low absorption. In addition, AlN is a good dielectric, is thermally and chemically stable and has high electrical resistivity which make it a suitable candidate for protective coatings and surface passivating layers of semiconductor surfaces [39]. Finally, thanks to its high *surface acoustic waves* (SAW) velocity it is of interest for the fabrication of electroacoustic devices such as bulk acoustic wave resonators, SAW filters, delay lines (widely used in TV, radio and telecommunications) [40].

The usual techniques for the growth of single crystalline AlN films: *Metal-Organic Chemical Vapour Deposition* (MOCVD) and *Molecular Beam Epitaxy* (MBE) require the use of high temperatures and expensive crystalline substrates that are not compatible with current semiconductor technologies for the fabrication of sensors. Reactive sputtered depositions is therefore the best option for the preparation of AlN films at low temperatures and lead to polycrystalline films with properties very similar to those of single crystalline films.

Fabrication

After cleaning the surface of deposition with HF 5% acid attack. Aluminium nitride has been fabricated by sputtering with an Aluminium target in an atmosphere of N_2 ($3sccm$) and Argon ($6sccm$) at a pressure during process of $4 \times 10^{-3} mbar$ and room temperature. Plasma easily formed in this conditions and was enhanced up to $200W$.

3.3.3 Carbon Nitride

Carbon Nitride was proposed by Marvin Cohen and Amy Liu [41, 42] in 1985, its theoretical prediction of a super-hard carbon nitride solid of composition C_3N_4 directed the efforts of many experimental groups to synthetise this compound. The research has been mainly focusing on synthesizing the hypothetical $\beta - C_3N_4$ (See Figure 3.5) which hardness would be close to that of diamond. It has the same crystal structure as $\beta - Si_3N_4$, with a hexagonal network of tetrahedrally bonded carbon and trigonal planar nitrogen. Besides its predicted hardness, carbon nitride is considered to be very promising in the fields of tribological and wear-resistance coating. In addition, carbon nitride may also be useful as electron emitters, variable band-gap semiconductors and transparent hard coatings. Due to this, huge efforts has been made to synthesize this new material using different techniques such as wave compression, high-pressure pyrolysis of organic compounds, but any of those have succeeded. Other attempts to incorporate nitrogen into carbon films were made by using a variety of techniques such as reactive sputtering, laser ablation, ion beam deposition, plasma-enhanced chemical vapour deposition. Recent research [44], however reported that 200nm size $\beta - C_3N_4$ had been achieved by reactive sputtering. Theoretical and experimental studies have proposed and discussed various nanocrystalline and amorphous structures leading to the formation of one, two, and three dimensional C-N compounds.

Fabrication

Its electrical resistivity varies widely with the nitrogen proportion in the fabrication process. Thus resistivity increases from 7.5×10^3 to 3.7×10^6 when the nitrogen fraction increases from null to 80%. It then decreases to 7.5×10^4 when pure nitrogen gas is used [44]. Hence to achieve the maximum resisitivity film diposits were made, sputtering various surfaces with a carbon target in a Ar/N_2 atmosphere with exactly the 80% of nitrogen (Nitrogen: $8sccm$, Argon: $2sccm$) and a process pressure of $5.3 \times 10^{-3} mbar$. To increase the adherence of the deposition on the wafer which had been previously attacked with HF 5% acid, it was heated up to $100°C(373K)$. However, plasma was not formed using this configuration. Instead, a 100% argon atmosphere allowed its formation and then, nitrogen proportion was gradually adjusted to the optimum. After that, sputtering power was set to $75W$.

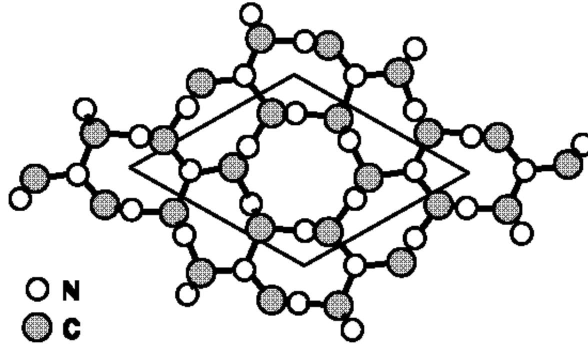

Figure 3.5: Diagram of Carbon Nitride $\beta - C_3N_4$ Source: [43].

3.4 Further work

The hot film anemometer meant to go onboard the MNL's is yet in early stage of design. Many improvements with respect the REMS wind sensor are still to be explored. General conception however has been already presented in this work and is likely to remain. If this is the case, some features could be included.

A metal layer above the insulating layer studied in this work could improve the resistance of the sensor to environmental conditions. Indeed, it would have almost no effect on the thermal and electrical behavior of the sensor due first to the underlaying electrically insulating layer and second, to the good thermal conductivities of metals in general. Indeed, it could help to further reduce temperature gradients over the surface of the sensor.

It has been considered to integrate a hot core inside the spheric structure of the sensor. This core would be heated to be at the same temperature than the platinum film. In this way, energy losses due to heat transfer between the surface and the rest of the sensor structure would be deeply reduced. This could cause, however, an increase of the overall power consumed by the sensor which is an important figure of the design.

In addition, it has to be decided which pattern of the platinum resistance deposited on the sphere would be optimum to minimize the existence of irregularities such as sharp curves which could cause hot points through the sector surface which in turn would create temperature gradients. Besides, this pattern should spread the energy uniformly through the triangular shape of the sectors.

Finally, as mentioned before, the dimensions of the sensor, that is, the diameter of the sphere, have to be set in order to fit laminar flow requirements while being the fabrication feasible. Hence it exists a trade off between dimensions, power requirements, and wind speed range of measurement which have to be still solved.

Chapter 4

Characterization

In this chapter the practical work performed along this project is described. The experiments carried out in order to choose the proper material from those explained in the previous chapter are presented.

First of all, those related to fabrication and characterization of the fabrication process. Although this does not contribute to solve the mean goal of this project, it provides useful information that might be valuable for further research about these materials with regards this or other projects.

Secondly, thermal measurements are meant to compare thermal properties of the materials pursuing a qualitative comparison within them. It has not been the purpose of this work to do a scientific characterization of the materials under investigation (such as in the case of many of the scientific publications referenced in previous sections) but to solve a specific engineering problem choosing the most convenient solution from those available.

Finally, electrical measurements have tried to demonstrate the insulating behavior of the actual fabricated materials, and subsequently the validation of the overall working principle by means of implementing a complete sigma delta control circuit working in CTA mode and simulating the effect of wind on the sensor with a fan.

4.1 Thickness measurements

Depending on the material different measurements methods have been employed:

1. Ellipsometry: used to measure SiO_2 thicknesses.
2. Profillometry: used to measure AlN and CN_x thicknesses.

An *ellipsometer* measures the change in the polarization of polarized light when the light is reflected from the dielectric - substrate interface. In general the change in polarization depends on the properties of both the film and the substrate. However in the simple case when the optical properties of the substrate are known and the film is transparent at the wavelengths being used, the change in polarization of the reflected light depends only on

Material	Process Press (mbar)	Ar (sccm)	N_2 (sccm)	O_2 (sccm)	t_n (min)
SiO_2	5×10^{-3}	5	0	10	60, 120, 180, 240
AlN	4×10^{-3}	6	3	0	15, 30, 60
CN_X	5.3×10^{-3}	2	8	0	15, 30, 60

Table 4.1: Processes performed in order to evaluate thickrates of sputtering depositions for different materials. The table shows the parameters used in the depositions and the different process times $(t_1, t_2, .., t_n)$. One deposition was made for each process time showed in the table.

the film thickness and index of refraction. The ellipsometer uses the first measurement to figure out the index of refraction of the deposited material and the actual thickness is obtained in a second measurement. Previous experience shows the adequation of this method to measure SiO_2 depositions. Hence, different sputter depositions of $SiO2$ have been analyzed using this technique (See Table 4.1).

On the other hand, the thickness measurement of AlN and CN_x depositions has been carried out using a profil

First a mask was created using Autocad. The pattern drawn has small motives spread in a whole 4 inches square (See figure 4.2). Second, the photoresists is adhered to the wafer following these steps:

1. Surface Cleaning: The wafer is chemically cleaned with acetone combined with ultrasonic agitation during 1 minute and then with propanol within another minute.

2. Dehydration Baking: The wafer is heated to 115ºC to drive off any water vapour on the surface during 5 minutes.

3. Resist *SPR-220* Application: Resist *SPR-220* is dispensed onto the wafer and then the wafer is spun at about 3000 RPM for 30 seconds to produce a thin uniform layer of $1.2um$ thickness. A spinner is used to this purpose.

4. Pre-bake: The wafer is again heated to 115ºC for 5 minutes and left during 25 minutes at room temperature.

5. Wafer Alignment and Exposition: The wafer is aligned with the mask slide and then exposed to ultraviolet (UV) radiation during 6 seconds.

6. Post Exposure Bake: The wafer is heated again to 115ºC for 5 minutes so that the *Photo Active Compound* (PAC) molecules can diffuse far enough to smear out in order to minimize standing wave effects along the edge of the resist, but not diffuse far enough to significantly distort the image features themselves. Hence, in this process, time control is critical.

7. Resist Develop *MF-24A*: A developer *MF-24A* is applied during 2 minutes.

8. Postbake: This is the final step in the photolithography and is designed to harden the resist and improve its etch resistance. It consist of a last heating up to 115°C during 5 minutes.

The next step of the process consist of performing various sputter depositions with the same parameters except for the process time. After the depositions are made, resist is attacked and removed so that material deposited on them is also removed and only remain on those zones without resist creating sharp profiles on the edges which are then measured with the profillometer as can be seen in Figure 4.1. This allow us to characterize the thickrate of the process for each target material by measuring the thick obtained by every deposition. The Table 4.1 summarizes the processes performed. The sputtered samples were then scanned by a *Dektak 150 Contact Profilometer* with the following setup:

1. Stylus Radius: 2.5um
2. Force: 3.00mg
3. Measurement Range: 6.5um
4. Profile: Hills&Valleys
5. Resolution: 0.10-0.30 um/sample

This characterization was necessary before starting all the other experiments in order to do depositions of different materials with approximately the same thickness. In the next sections therefore deposition layers of around 150nm have been fabricated independently of the material used.

4.2 Thermal measurements

Thermal measurements were carried out using a *Model 218 Temperature Monitor* that can be used with diode or resistive temperature sensors. It can manage a maximum of eight inputs. In our case four inputs were used at the same time. Hence four platinum resistances temperature sensors *Pt1000* were connected to the device using a 4 wires configuration and soldering them to the device pins according its manual instructions.

IE-488 computer interface were used to communicate with LabView 8.5. In addition, a virtual instrument was created to store and graphically show temperature measurements of the four sensors in a synchronous way. This virtual instrument used in turn virtual instruments and drivers provided by the manufacturer to manage device configuration and data acquisition. Hence in four channels, GPIB address was set to 12, Inputs group to 1-4, Input type to "5k Ohm Platinum" that is suitable for *pt1000* both in type and range, Data source was set "Celsius" and finally Input Curve to "pt1000". Block diagram of the virtual instrument can be seen in Figure A.1.

First, described options are the input of the *LSCI 218 InPUT* block. Second, a timer sets a wait time of 1 second so that information can be successfully sent to the device

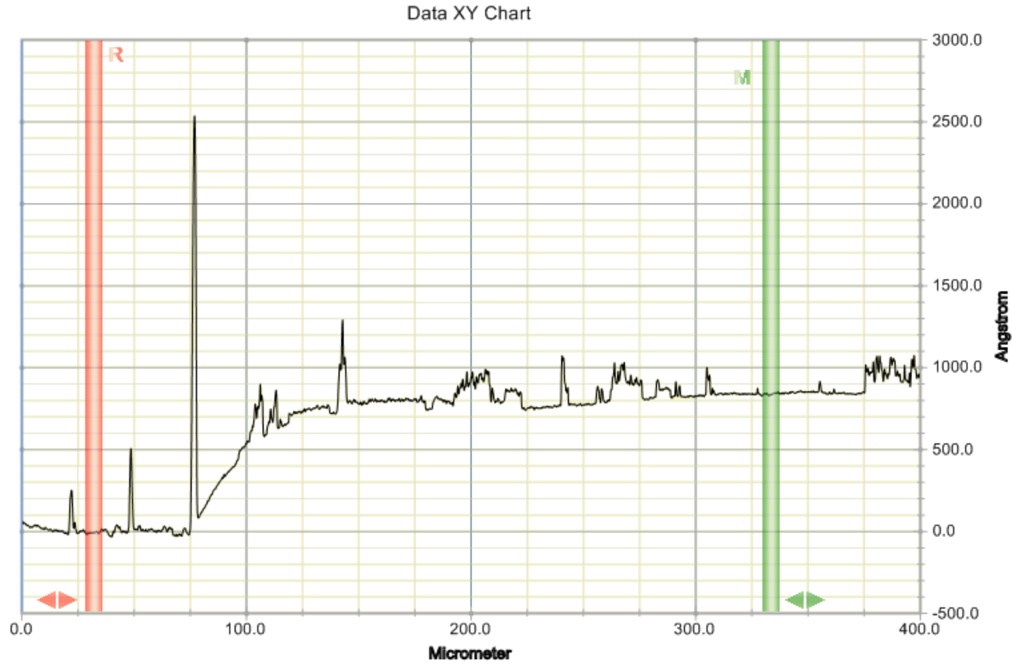

Figure 4.1: Plot given by the profilometer measuring AlN deposition thickness.

and properly processed. Third, *LSCI 218 Read Meas* perform the actual reading of the device display. Measured temperature is then ordered so that can be easily shown in a thermometer and plotted in a chart. This diagram is repeated four times for simultaneously process and represent data coming from the four different channels in four different charts and thermometers. Finally, all the blocks are placed in a general loop which periodically update data until stop button is pressed.

A hot plate was used in all thermal experiments. Its temperature was set to 80°C before starting the experiments. Temperature of the plate was controlled and supplied by a *Signatone model S-1045* and cooling was supplied by a *Coolflow CFT-33* refrigerated recirculator. The experiments always consisted of analyzing temperature change of the devices under test when they were left on the hot plate so that heat conduction increased the temperature of those. It was assumed that only conduction occurred, that is, convection to the air was neglected. Hence more accurate results would have been obtained if experiments were done in a vacuum chamber.

4.2.1 Silicon Wafer depositions

In this case, a silicon wafer was cut into four different square dice of 15mm of side each. After removing native oxide with 5% HF acid during 30 seconds, three of them were then sputtered with SiO_2, AlN and CN_X respectively to obtain diposits of 150nm approximately. No deposit was made to the fourth die. The four pieces of silicon were placed in a thin metal plate and four temperature sensors *Pt1000* were placed over them in contact

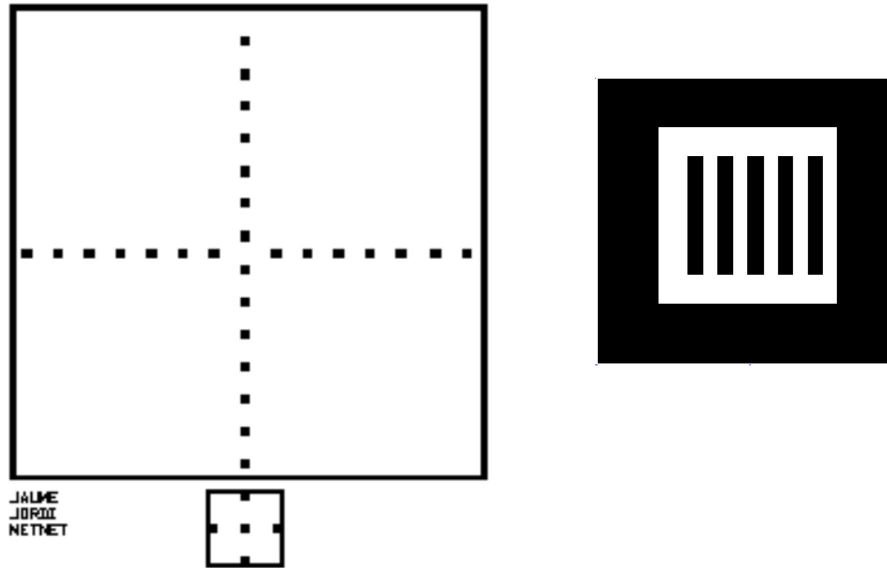

Figure 4.2: Overall view of the mask created with Autocad. In the left part of the image, at the top a 4 inches square, and at the bottom the little motive meant to characterize the process with little pieces of silicon wafer. At the right part an insight of the littles squares showing its internal pattern.

with the diposited material. The thin metal plate was then settled on the hot plate at 80ºC and increase in the temperature of the deposited material was measured. Thermally, this is equivalent to the application of a heaviside impulse function $u(t)$ to the thermal system. Thermal response of the system can be therefore evaluated at the output wich will be of the form $h(t) * u(t)$. Neglecting the dynamic effect of the thin metal plate (which is equivalent to suppose that heating is transmitted instantaneously through it) thermal system will be a second order linear system whose transfer function in Laplace domain will contain two real poles placed in frequency at the inverse of the time constants of each pole. As shown in Section 2.1 this system will be always overdamped and hence response in time domain will be exponential. Since variables such as material thickness and square dimensions have been controlled, it is expected therefore that depositions will slow down its time response with respect to the die without any deposit depending only on the thermal diffusivity of the different deposited materials.

To neutralize possible differences between the four temperature sensors sensitivity as well as non uniform temperatures of the hot plate along its radius, the assay was repeated four times permuting the silicon samples allocation each time while keeping temperature sensors in the same place. Later on, mean values have been taking of all the measurements and times responses have been then compared.

4.2.2 Teflon depositions

In the experiment explained before, thermal energy is serially conducted, first through the silicon wafer and second, through the material deposition. Although the thermal diffusivity of Silicon is relatively higher ($0.8cm^2/s$) compared to that of the deposited materials (See Table 3.1) since the thickness of the wafer ($100\mu m$) is much bigger than that of the deposition of interest, overall dynamic response is mostly determined by the silicon wafer which masks the effect of the deposition. Therefore, only small variations can be measured as a result of the thermal diffusivity of the different deposits made.

In order to increase the effect of the depositions, the following experiment is carried out.

Three bars of *Polytetrafluoroethylene* (PTFE/Teflon), which is well known for its poor thermal diffusivity ($15 \times 10^{-6}cm^2/s$ [45]) compared to those of the materials under investigation (See Table 3.1), were carefully cleaned with propanol and then sputtered with $150nm$ thin films of SiO_2, AlN and CN_X respectively. Teflon bars were manually cut and had equal dimensions ($30mm \times 10mm \times 1mm$). A fourth bar was used as a reference without any deposit as made in the first experiment.

During the experiment $10mm$ of the deposited side of the bar were in direct contact with the hot plate. The next $10mm$ were a free path without any interaction (neglecting convection with air). Finally, at the opposite $10mm$ of the bar, the temperature sensor $pt1000$ was placed in direct contact with the deposited material.

In this case the thermal system can be modeled as two impedances placed in parallel circuit configuration where that of the Teflon is relatively much bigger than that of the deposition and therefore its effect on thermal conduction can be neglected as a first approximation.

It is expected then that heat will be conducted along the deposited material and will reach the platinum sensor. Time response measured by them will mostly depend on thermal diffusivity of the material deposited.

Four Teflon bars were placed simultaneously to ensure that results were comparable. Besides, in the same way than the previous experiment, the process was repeated four times permuting the bars location with respect the temperature sensors, and therefore avoiding possible differences in sensors behavior.

An important note about this experiment is that previously to the use of $30mm$ long bars, the same experiment was tried with $60mm$ long bars, but temperature changes could not be observed at the opposite side of the bar this way. Unfortunately this behavior suggests that while poor conductive, Teflon absorbs an important part of the thermal energy avoiding its transfer through the deposited surface to the temperature sensors. Although this is not critical to our experiment since it happens equally in all the bars and comparison is still possible, it would make impossible a quantitative evaluation of thermal properties of the materials tested this way.

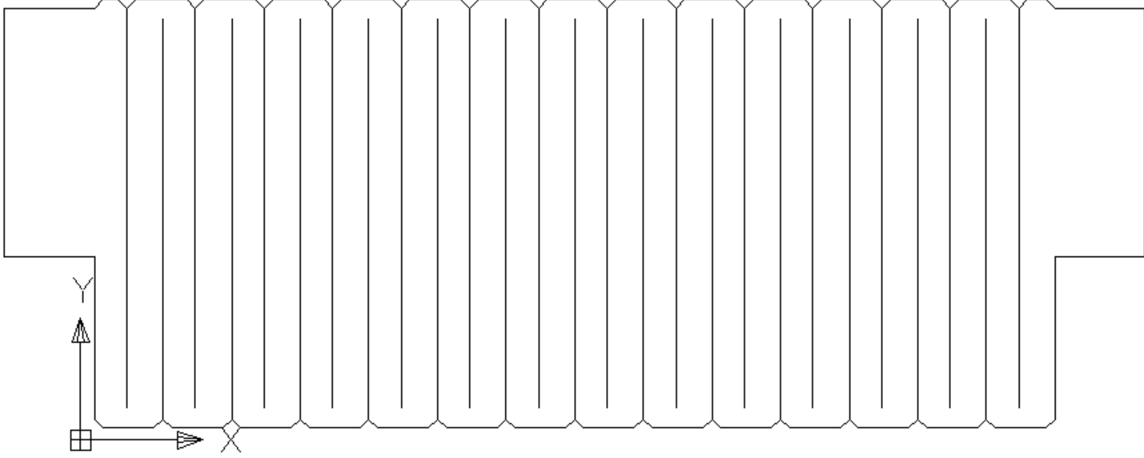

Figure 4.3: Autocad plot used by the laser to cut the platinum resistance deposited. Ninety degrees corners have been avoided the presence of hot points. Published with the permission of Samir Kassar.

4.3 Electrical measurements

In this section electrical measurement carried out during this project are described. First of all, electrical resistivity of the insulators was measured. However, available equipment was not suitable to measure high resistivity values. Nevertheless, these results showed without doubt the highly insulating behavior of the materials which is in agreement with the design requirements.

Subsequently experiments dealt with the functionality of the hot film anemometer itself. To do so, other virtual instruments were implemented making use of a power supply *Agilent E3631A* and a multimeter *Keithley 2000* both being equipped with IEE-488 computer interface. The devices under test were $100nm$ thick platinum resistances sputtered over a glass support with a surface of $210mm \times 480mm$ and cut with a laser beam to form the resistance pattern designed with *Autocad* and shown in Figure 4.3. After that, depositions of the $150nm$ thick insulating layer were made by sputtering of SiO_2, AlN and CN_X over the platinum resistance. Finally, to evaluate the effect of wind on the electrical measurements a fan was used at a constant distance from the device under test.

4.3.1 Electrical Resistivity

Isolation materials described in this work were already chosen due to its high electrical resistivity. Hence, in the case of SiO_2 ($\rho_e > 10^{12}\Omega cm$), in the case of AlN ($\rho_e \approx 10^{10}\Omega cm$), and ($\rho_e \approx 10^6$) in the case of CN_X. However these theoretical values can widely change depending on contamination and the crystalline structure formed during the fabrication of the compound. In this work estoichometry or crystal structure of the depositions have

been not analyzed after the fabrication. Hence it has to be checked if the theoretically high electrical resistivity of the materials persisted. To do so sputter depositions of $150nm$ thick on different surfaces were used.

The first measurement was made with a *four point probe* to measure square sheet resistance which is defined as:

$$R_{sh} = 4.53\frac{V}{I} \tag{4.1}$$

being $4.53 = \frac{\pi}{\ln 2}$ the so called *correction factor*. From here, resistivity is easily deduced knowing the thickness of the deposition t:

$$\rho_e = R_{sh}t \tag{4.2}$$

However, in all cases the power supply did not have enough voltage ($V_{max} = 24V$) to keep a non zero value (according to the multimeter sensitivity $\approx 10nA$) of current through the material. Although this result is not enough to provide a quantitative measurement, it shows that resistivity must be higher than (taking into account that deposition thickness was $\approx 150nm = 150 \times 10^{-7}cm$):

$$\rho_e > 150 \times 10^{-7} \times 4.53\frac{24}{10 \times 10^{-9}} \approx 10^5\Omega cm \tag{4.3}$$

Alternatively, the ohmmeter of the $Keithley$2000 was used over the deposited sensor on the glass support described before to do a regular two wire measurement as follows: One terminal was located in direct contact with the Platinum, in the specific place meant to make the wirebonding so that no insulator had been deposited, the other was located over the insulating material deposition. Roughly speaking, the resistance measured in this way can be related to resistivity of the insulating material with this expression:

$$R = \rho_e\frac{t}{A} \tag{4.4}$$

being R the measured resistance, t the thickness of the deposited material ($\approx 150nm$) and A its area ($21mm \times 48mm$). Resistance values were measured for AlN and CN_X, which did not happen in the case of SiO_2.

4.3.2 Open loop test

The purpose of this experiment was to analyze the response of the platinum sensor resistance when wind was applied to it depending on the insulating deposited interface. As explained before, four support glasses have been used, three of them with the respective material sputtered on it and the last one with just the platinum layer.

A simple virtual instrument was created with LabView to control the multimeter and store its voltage data measurements in a chart (See Figure 5.6). The $5V$ output of the power supply was set to work as a current source which was set to $100mA$. In the case of the SiO_2 sensor, this gave a constant voltage of $3.94V$ which is a resistance value of 39.4Ω and

the CN_X sensor, this gave a constant voltage of $3.65V$ which corresponds with an electrical resistance of 36.5Ω. In the case of the AlN sensor, due to some defect (like a scratch) on the platinum deposition resistance was quite bigger (up to 650Ω) so that the $24V$ output of the power supply had to be used in order to work as a current source similar to that of the other two sensors, in this case of $36mA$. Since the variable to characterize is the time response, different working points, that is, sensors temperature due to autoheating, should not make a difference as a first approximation. Finally, in the sensor where not deposition was made $100mA$ were applied and the voltage obtained was $1.44V$ which is given by a resistance of 14.4Ω.

Resistance differences between sensors must be produced not by insulator layers, which is equivalent to a high impedance in parallel to the platinum so that it can be neglected, but to possible differences in the platinum deposition itself such as different thicknesses or possible defects produced after the fabrication process. This should be taken into account when the final designed is fabricated because it might be necessary some calibration system so that exact values of the resistances sputtered would not be critical.

Thermally the application of constant wind to the sensor is equivalent to a step function u(t) applied at the output of system analyzed in Section 2.1. Hence four decreasing exponential curves of the time-depending tension difference in the platinum resistance were obtained. Time constants of these step responses have been analyzed and compared.

4.3.3 Closed-loop validation

Finally, the closed-loop validation has been performed in order to ensure the general feasibility of the depositions. To do this, a complete sigma-delta control circuit has been implemented to test the sensor functionality in a digital CTA operation mode. The experiment setup consisted of three parts:

1. A Wheatstone bridge was implemented in a breadboard. The two resistances at the low part of both branches of the bridge were 10Ω resistances. At the higher part of one of the branches a 1000Ω multiturn potentiometer was placed, at the other one the sensor under test (the glass support described before) was connected. To do so, two wires were previously soldered two the sensor wire pads. The potentiometer has been adjusted so that the bridge is balanced, that is, error voltage at the output of the bridge is minimized.

2. The rest of the CTA configuration has been implemented by means of the multimeter in one hand, the power supply on the other hand, and a virtual instrument (See Figure A.2) implemented with LabView which controlled the equipment using IEE-488 interface. This virtual instrument first sets the proper configuration in both devices using the virtual instruments and drivers provided by the manufacturer. After that an infinite loop has been created which plots current value and output voltage while comparing this value to a preset adjustable threshold which determines whether to switch from ON (high current value) to OFF (low current value) mode

or not and the other way around. However a timer was used to allow the power supply and the multimeter to properly communicate and process messages. This means that the multimeter has been used to measure the voltage error at the output of the bridge and the power supply has been used as current source operating at two possible current values I_{on} and I_{off}. Hence the block that closes the loop is the comparator which sets the future state of the current source. The frequency of the clock is limited by the latency of the power supply to change the current state to $0.8Hz$ approximately. Finally, the circuit state itself can be seen as a digital readout of the wind velocity being the relative probability of the state ON with respect the state OFF an indirect measure of wind speed.

3. A desk fan have been used to perturb the equilibrium of the control circuit during a determined period of time. Hence it is the step function $u(t)$ that desestabilizes the sensor resistance and therefore the balance of the bridge. Distance between the sensor and the fan has been kept constant in all experiments. Besides, the distance between the fan and the rest of the elements of the bridge has been carefully maximized. In fact, it has been clearly observed that wind also modifies resistance of the potentiometer as well which distorted the circuit operation.

The procedure of operation consisted firstly of setting a very high value of the threshold and therefore making the circuit operate always in ON state. Then the potentiometer was adjusted to set the output voltage of the bridge to a small value, say $10mV$ for instance. Then the threshold is placed just under the bridge output and the circuit starts oscillating (switching from ON to OFF and so on) around this value. However, as time passes, the increasing temperature due to autoheating changes the voltage values and slight adjustments might be necessary before it reaches the stationary state. Once this happens, the fan, conveniently placed over the platinum sensor, is switched on during 25 seconds. This makes the output voltage of the bridge continuously fall in both states, and when the first high value falls under the threshold, the state is held until the threshold is passed, the circuit can need two or more clocks to reach it. At this point, ON/OFF ratio starts to increase. There is a certain ratio at which the control circuit stabilizes again. In the same way, when the fan is switched off, output voltages of the bridge start rising again in both states, and it gradually returns to the previous stationary status.

This process has been repeated four times for each glass support. However, in the same way than in the previous experiment, when the anemometer sputtered with AlN was used, its high resistance made necessary to change the bridge resistances. Hence 10Ω resistances were removed and 100Ω resistances were placed instead. Furthermore, the power supply output had to be changed to the one of 24V and multiturn potentiometer was heavily adjusted. Although this changed the order of magnitude of the threshold, the similarity between the powers supplied to the bridge ($P = RI^2$) makes plausible a similar temperature due to heating of the resistance and therefore a similar time response despite the change produced but the insulating layer.

Chapter 5

Results and discussion

In this chapter, results of the experiments and characterization processes explained in the previous one are presented. Some charts and tables are included to illustrate the explanation. They are described and discussed as well, in other words, they are compared with *a priori* expected behavior, and some intermediate conclusions are deduced. These will lead to the final conclusions relevant to the objectives of the work which will not be given until the next chapter though.

Thickness rate of sputter deposition of the materials under test were studied. The ultimate objective of this analysis is to be able to make different material depositions of the same thickness in order to compare more accurately their properties. Indeed, after this characterization, several deposits of approximately 150nm thickness were fabricated. Thus, according to fitting curves shown in Figures 5.1, 5.2 and 5.3, where the results of the processes described at Table 4.1 are graphically represented, thickrate of AlN deposition at 200W is $1.95nm/min$, thickrate of SiO_2 deposition at 200W is $2.23nm/min$ and thickrate of CNx at 150W and 100°C is $45nm/min$. In addition to the actual experimentally measured points, the trivial zero point which represents the fact that no deposit is made in 0 time was used to compute the fitting curves. On the other hand, the fitting curve was not soldered to that point so that its slope better reflects the mean thick rate along all the time intervals which is, probably, not completely constant.

It is interesting to point out the differences between the rates of AlN and SiO_2 and that of CNx which is significantly higher. The main reason to this behavior could be the crystalline nature of the Al and Si targets whose chemical bonds are stronger than those of the amorphous C target.

These differences made necessary to reduce the power of the C depositions to a half so that the deposit could last between 5 and 10 minutes to achieve the same thickness than that of 60 minutes deposits of the other two materials.

It is important to note that all the processes were made while the wafer was rotating in the chamber to minimize thickness gradients within the wafer surface. However, they are not null and mean values were taken of the different measurements made with profilometer along the deposition pattern created by photolitography (See Figure 4.2). Indeed, when 5 inch wafers were deposited at once differences turned out to be much higher. The worst case

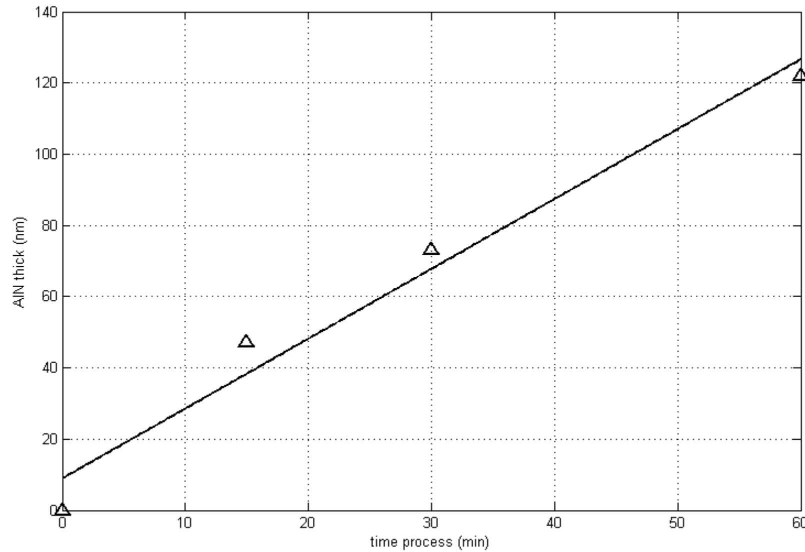

Figure 5.1: Thickness measured for different processes time of AlN deposition at 200W and room temperature.

happened in the deposition of CNx in 5 inch wafer which was carried out at temperature and therefore rotation was not possible (due to design limitations of the sputter chamber) and distance between the target and the sample was smaller compared to the maximum distance used in the other depositions. Due to all these reasons, only cut small pieces of wafer were taken into account and they were always carefully located at the center of the chamber.

Furthermore, it is important to mention that there was no previous experience in the case of AlN and CNx sputter depositions. Only bibliographical sources, which tend to be not enough explicit as far as deposition parameters are concerned such as time, power, wafer temperature or process pressure, were used as a first approximation guide to perform the deposits. Hence, the value of these charts 5.2 and 5.3 represent a new knowledge for the particular case of the clean room which could be used as a reference in the future for further research or fabrication of these materials. Nevertheless because of the reasons mentioned before, thickness should be measured for every particular sample to check its real thickness.

In Figure 5.5 results regarding thermal measurements, carried out with depositions over silicon wafer, are shown. The setup and procedure followed to obtain these curves is explained in Section 4.2. Each one of these charts, of a total of four, shows four exponential curves inside, in different colors, which are obtained in a single experiment, that is, when the same step function is applied to the four corresponding samples: Wafer, Wafer + SiO_2, Wafer + AlN and Wafer + CNx. The legend under the charts determines the relation within the curves and the material deposited by means of different colours.

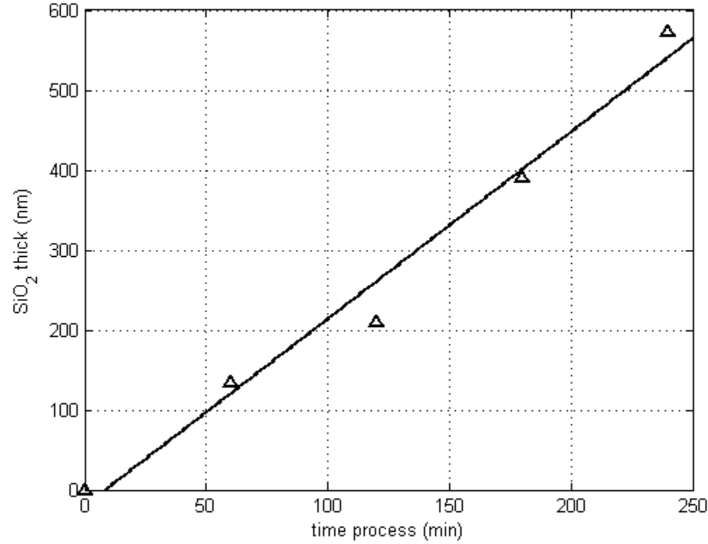

Figure 5.2: Thickness measured for different processes time of SiO_2 deposition at 200W and room temperature.

In all cases the time duration of the chart is set to 100 seconds. However the starting point varies from one to the next. The slight decline of the temperatures at the end of the curves is due to the fact that the hot plate temperature, which has been set at 80°C from the outset, had a slow but constant decline along the time. However this effect is far from modifying the results obtained.

It can be seen that differences in the results of the four charts are important. For instance, the final temperature value order is different in all the cases. This demonstrates that there is an important biasing in the experiment due to deviations in the particular behavior of each of the *Pt1000* temperature sensors. Although it is not clear that time response can be affected by the sensitivity of the sensors, which depends on its linearity, that is, whether the sensitivity is constant along the range of measurement or not, the repetition of the experiment, permutating the sensors used in each case, turns out to be completely necessary to control this variable and remove the possible biasing from the measure. Therefore mean value of the time constants are taken in Table 5.1.

As expected, wafer alone shows a fastest time response of $\tau = 10s$ which is coherent with the overdamped low pass filter thermal model mentioned several times along the present work. Moreover, AlN shows the fastest response $\tau_{AlN} = 12s$ within those with deposited material. This is also an expected result due to the high thermal diffusivity of this material compared to the others (See Table 3.1). The other two materials show equivalent responses that are quite longer: $\tau_{SiO_2} = \tau_{CNx} = 15s$.

However, in general, time results seem to be greater than those expected according to their thermal resistance, heat capacity and thickness (See Equation 3.14). It might be due to the intrinsic time constant of the thermal sensors which according to the literature

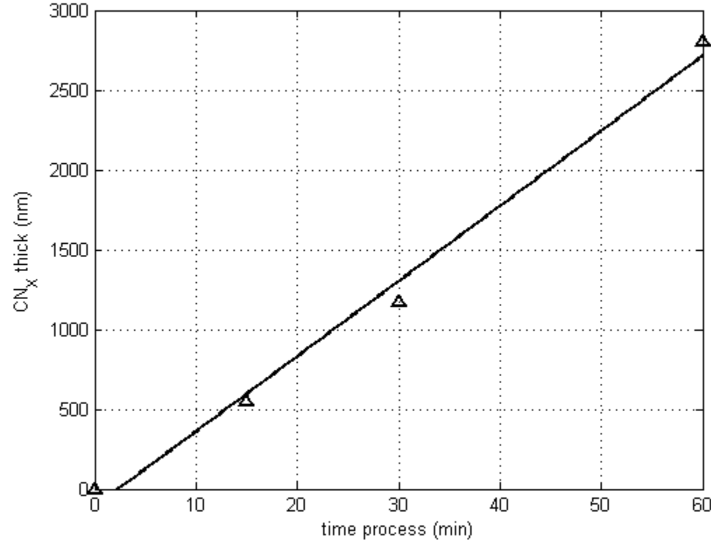

Figure 5.3: Thickness measured for different processes time of CN_X deposition at 150W and 100°C temperature.

Material	τ_1 (sec)	τ_2 (sec)	τ_3 (sec)	τ_4 (sec)	τ_{mean} (sec)
wafer	9	12	9	8	10
wafer+SiO_2	16	17	13	12	15
wafer+AlN	12	13	14	10	12
wafer+CN_X	14	18	15	12	15

Table 5.1: Time responses of the thermal system composed by different material depositions over a silicon wafer. They are shown for the four repetitions of the experiment and in the last column the mean value is computed.

use to be between 3 and 8 seconds. This parameter has not been characterized in this work. By the way, this parameter can be different from one sensor to the next. Anyway, this error results in an increase of the whole thermal system time response which should not affect the comparison among the different materials once the mean values of the four permutations have been computed.

In addition, convection to the air, which can be modeled electrically as a thermal resistance to grown, could affect the final values of the exponentials which in all charts are far below the 80°C supplied by the hot plate. This effect once again is the same for all the depositions and therefore should not affect the comparison.

Regarding the thermal measurement carried out with the materials deposited over Teflon, results can be seen In Figure 5.5. In the same way than before, four curves are shown in every chart, of a total of four. Colors can be related then to corresponding materials thanks to the legend below the charts. Now, time responses are much longer,

Material	τ_1 (sec)	τ_2 (sec)	τ_3 (sec)	τ_4 (sec)	τ_{mean} (sec)
teflon	24	26	16	43	27
teflon+SiO_2	31	23	22	22	25
teflon+AlN	20	30	24	21	24
teflon+CN_X	24	18	31	25	25

Table 5.2: Summary of Figure 5.5.Time responses of the thermal system composed by different material depositions over a piece of Teflon. They are shown for the four repetitions of the experiment and in the last column the mean value is computed.

and temperature differences before and after the application of the step function, the direct contact with the hot plate, are significantly reduced. One more time, result variations among the four charts justify the sensor permutations.

In table 5.2, mean time constants of thermal system described in Section 4.2.2 are shown. AlN appears to be again the fastest material with a time response of 24s. Furthermore, as expected from the lower thermal diffusivity of Teflon compared to that of the other materials under test, its thermal response is the longest with 27s. However, the difference between this and that of the rest of materials (time response of both SiO_2 and CN_X is 25s) is not as important as it was foreseen according to differences in thermal diffusivity (several orders of magnitude). One reason to explain why this is so, could be that heating is absorbed by Teflon due to its bigger volume and mass and that heating of thermal losses through the structure of the setup and convection to the air are much higher when time constants are longer which therefore diminishes the differences within the results, so to speak. In this case, final temperatures are about 30-40°C which is approximately 30°C below the final temperatures obtained in the previous experiment and about 50°C below the temperature of the hot plate. Total variation in temperature due to the step function is between 10-15 degrees while in the previous case this variation was up to 35 degrees in some cases. These differences suggests that heat losses are much higher now.

As far as electrical measurements are concerned, resistance values could be measured following the procedure described in Section 4.3. Resistance and the corresponding computed electrical resistivities are shown in Table 5.3. They are in agreement with the high electrical resistivity theoretically predicted. As for the case of SiO_2, although no value has been obtained, this only means that the equipment used was not enough to measure such a high resistivity value.

In Figure 5.6 can be seen curves obtained measuring fall in voltage when the wind produced by a fan is applied to each hot film sensors previously fabricated using platinum and a coating of the different materials under test. In fact, since current is kept constant, a fall in voltage demonstrates that resistance decreases by cooling due to an increase in convection to wind. As mentioned in the previous chapter, room temperature resistance of the four samples of sensor sputtered differ in value. The bigger the resistance is, the bigger is the falling tension for a given current. In the case of the sample sputtered with AlN happens that resistance is around ten times bigger than the rest so that an inferior

Material	R (Ω)	ρ (Ωcm)
SiO_2	-	-
AlN	1.5×10^6	$\approx 10^{12}$
CN_X	≈ 20	$\approx 10^5$

Table 5.3: In First column the name of the material is shown, in the second column the resistance value measured, and finally the estimated electrical resistivity is presented in the third column. First row is empty because the measurement exceeded the range of the multimeter.

Material	I(mA)	ΔV (%)	τ
Pt	100	-2.77	21
Pt+SiO_2	100	-1.42	18
Pt+AlN	35	-3.35	15
Pt+CN_X	100	-0.82	30

Table 5.4: Summary of Figure 5.6. In First column the current supplied is shown, in the second column the total fall in tension in relative terms (which is in turn equivalent to the fall in resistance value) and, finally the time constant of the thermal system composed by the platinum hot film and the thermal isolator hot film.

current value has been applied so that voltage is kept in a reasonable interval which can be achieved by the power supply. Hence, $100mA$ has been applied in all cases except in the case of AlN where current has been set to $35mA$. In Table 5.4 proportional variation of tension is shown. The maximum variation is the one of AlN with -3.35%, followed by the one without coating with -2.77%, then the one of SiO_2 with -1.42% and finally CN_X with a variation of -0.82%. It can be deduced from this that sensitivities of the sensors to speed of wind widely vary depending on the material used. Surprisingly, AlN somehow manages to increase the sensitivity with respect the Platinum alone. However, it might be taken into account that AlN probe is hotter than the others and that its temperature distribution could be heterogenous which is deduced from its strange high resistance value. This could lead to a different thermal interaction.

Anyway, time constants, also shown in Table 5.4, have greater interest. One more time, AlN probe shows the best performance with $\tau_{AlN} = 15s$. Once again, AlN is faster than Pt alone, $\tau_{Pt} = 21$, which is surprising as well. This time however, it can only be due to a better convection of the AlN layer with air and a faster conduction through all the platinum surface which in effect makes faster its dynamic response. In this case, SiO_2 beats Pt as well with a time constant of $\tau_{SiO2} = 18$. The slowest response corresponds to the CN_X probe with a time constant that doubles that of AlN, $\tau_{CNx} = 30$.

Despite the fact that these results have been obtained under the same conditions and are therefore valid, it might be necessary to reproduce them with several probes of each material to ensure that this behavior is not due to some uncontrolled parameter. Indeed, a quantitative characterization of the materials analyzed would have required the use of

equipment and procedures not available for this thesis. Regardless the objections that have been pointed out, all the experiments performed so far point to an univocal conclusion: *AlN* behaves much better than the rest of materials in terms of thermal propagation, which is, by the way, what theory predicts. As mentioned in the introductory chapter, the scope adopted in this work has been the comparison of the different sputtering target materials available at the clean room in order to choose between them the one that best suits the needs of the design: high thermal conductivity and high electrical resistivity.

The experiments carried out in this work altogether therefore reflect from different points of view the expected behavior of the hot film probe in real operation.

Finally, the effect of wind in close loop CTA configuration is shown if Figure 5.7. The frequency of operation has been limited by the power supply which can change its current supply once per second approximately. The charts show the voltage error at the Wheatstone bridge described in Section 4.3.3 for each deposited material. It can be observed as well the switching of current value between *ON* state and *OFF* state. The system has been calibrated so that both states are equally probable in equilibrium. When wind is applied during 20 seconds, *ON* states are more abundant than *OFF* states therefore compensating the temperature diminution of the sensor and hence keeping it constant. Besides, it appears clear now that a windowed mean of the current can be used as a direct read out of the wind speed since the faster is the wind, the more frequent will be the *ON* state with respect the *OFF* state.

Oscillation of voltage around the threshold would be minimized increasing the frequency of operation. In a real calibration of the sigma delta circuit, *OFF* states should be more frequent than *ON* states in equilibrium which would enhance the dynamic range of wind speed measurement. However this closed loop validation has been meant only to prove the stability of the hot film designed and has been successful.

Again it can be observed, that the most sensitive material against wind is *AlN* causing the biggest fluctuation in voltage error. However, it should be taken into account how this affects to the overall range of operation of the sensor because, in this case, small fluctuations in wind speed create big fluctuations of the sensor resistance which was shown previously in Table 5.4 with a greater relative decay of voltage than the rest of materials.

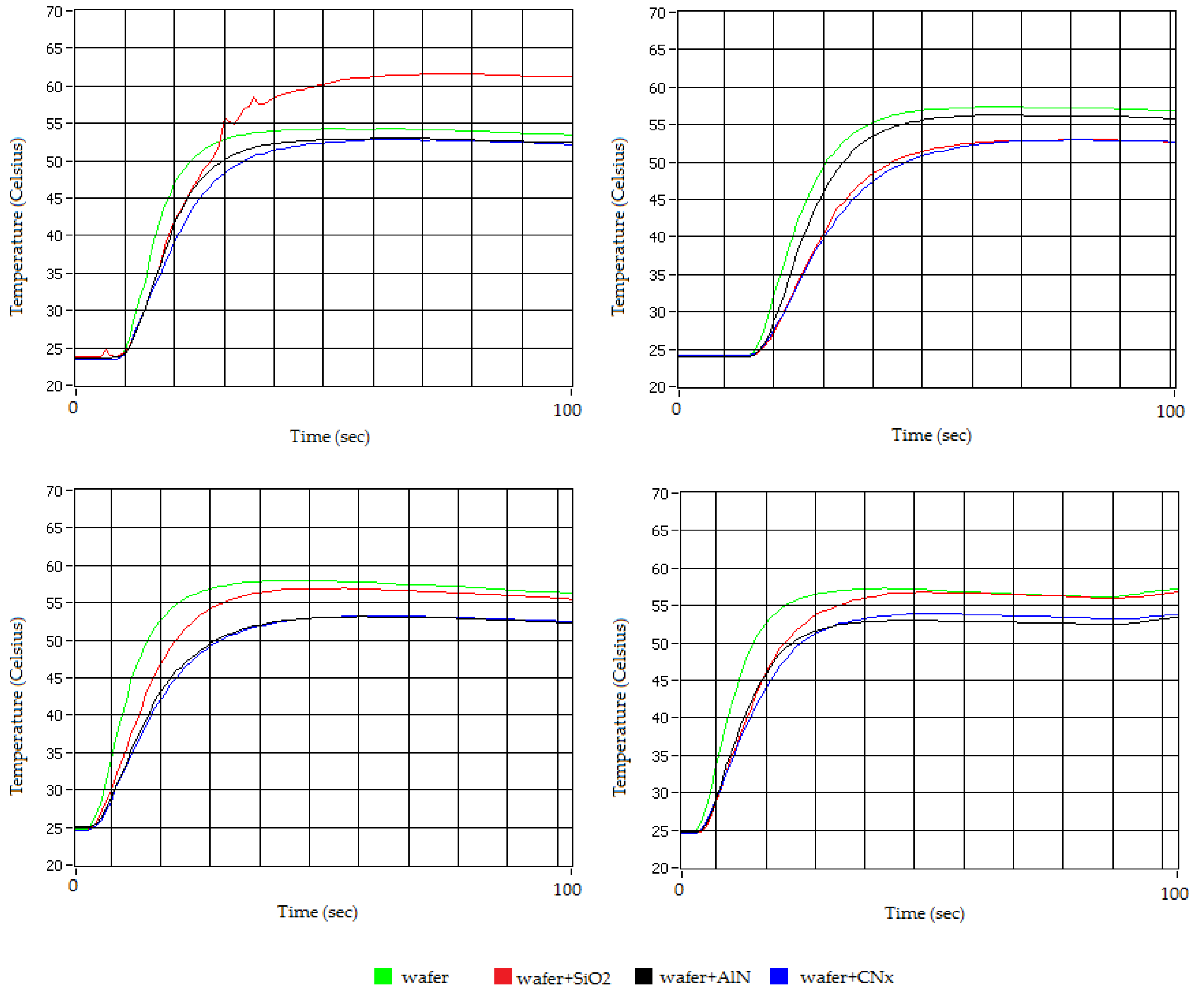

Figure 5.4: This four plots show the step response of the different material depositions over a common silicon wafer when put simultaneously over a hot plate at 80°C. Each color represents one material as indicated in the legend. Each chart correspond to a single repetition of the experiment with different permutation of the *PT1000* thermal sensors in order to control possible differences between them.

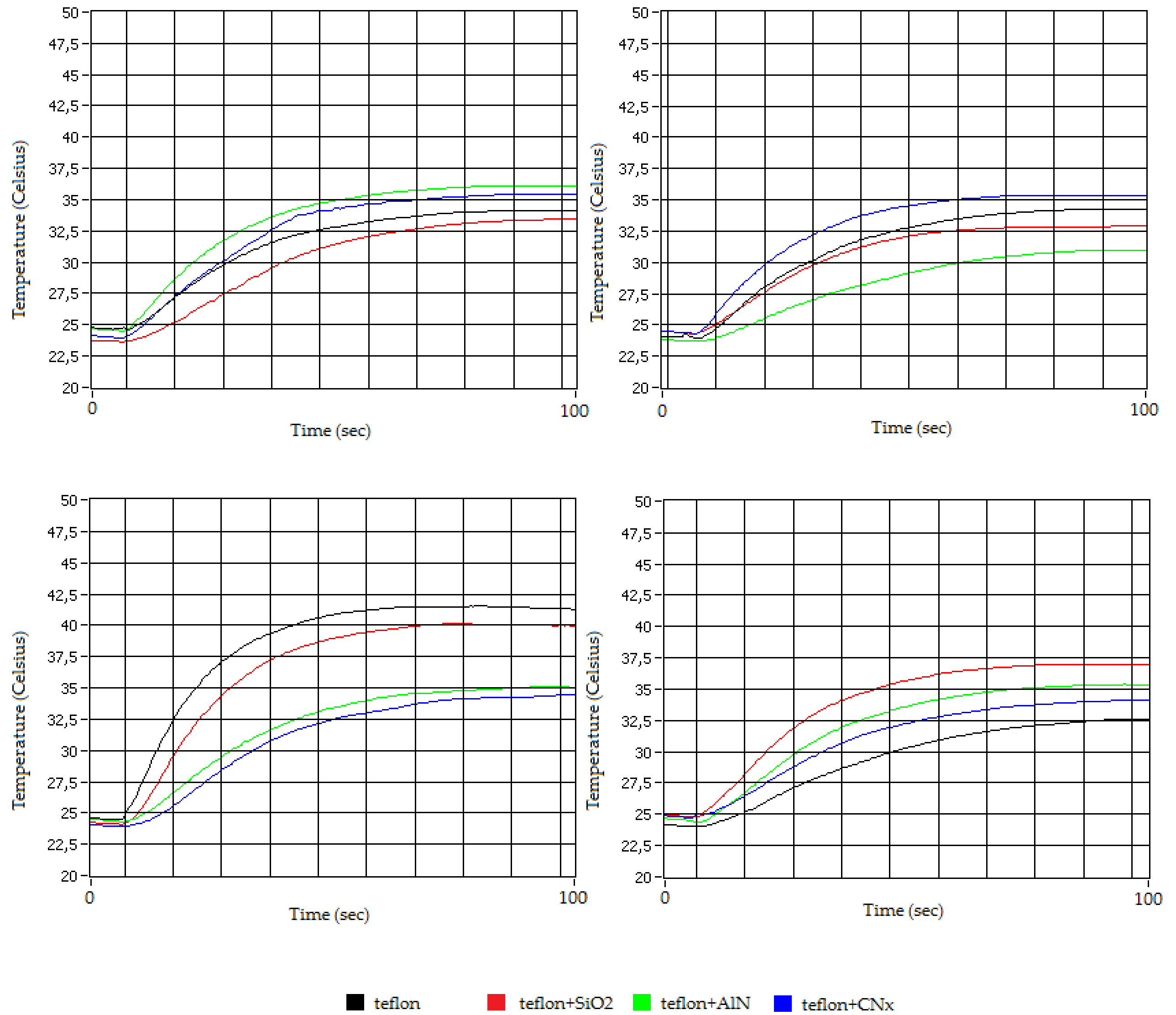

Figure 5.5: This four plots show the step response of the different material depositions over a common Teflon surface when put simultaneously over a hot plate at 80°C. For more details about the experiment see Section 4.2.2. Each color represents one material as indicated in the legend. Each chart correspond to a single repetition of the experiment with different permutation of the *PT1000* thermal sensors in order to control possible differences between them.

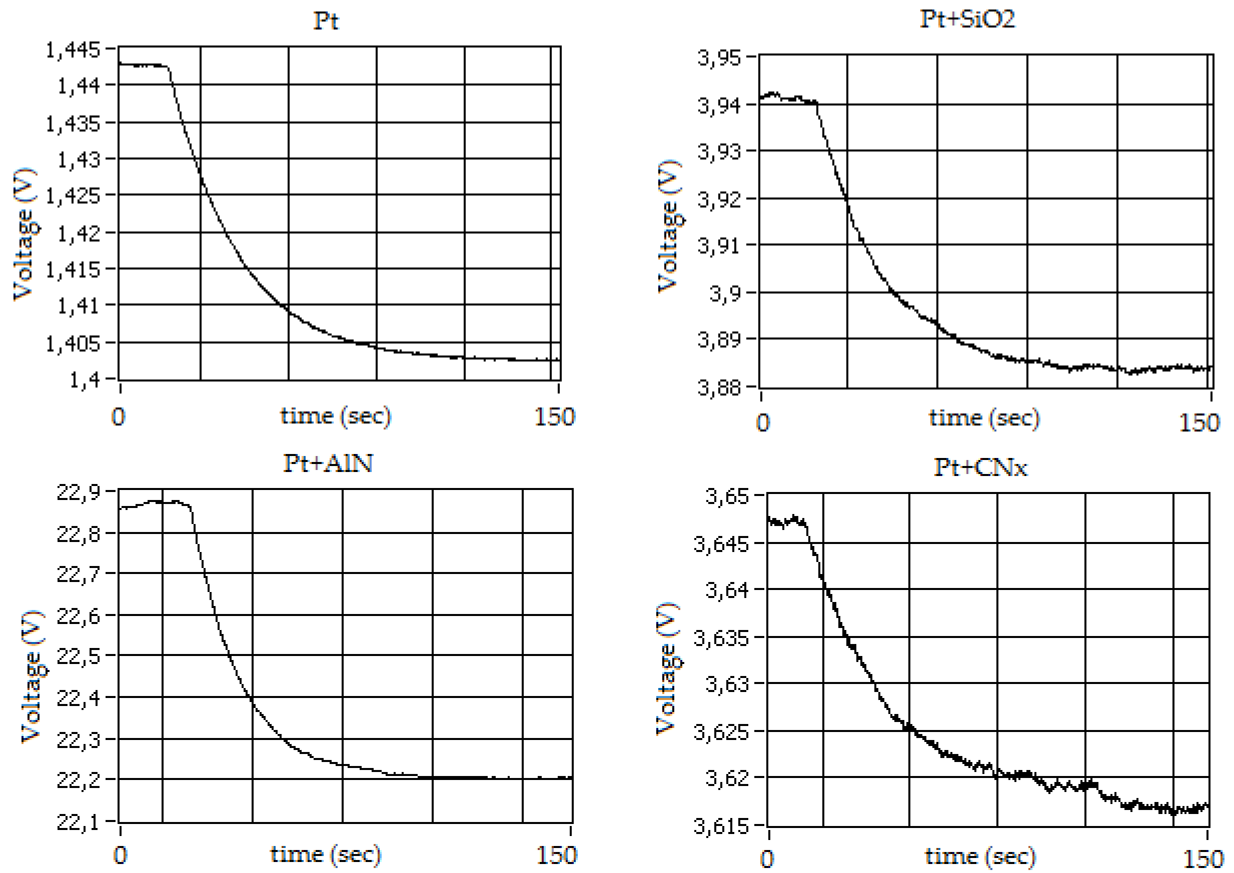

Figure 5.6: This four plots show the step response of the different material depositions over the actual hot film anemometer and connected to a current supply (open loop configuration) when cooled by wind produced by a fan placed at a certain distance from the probe. In all cases current is $100mA$ except in the case of AlN where is set to $35mA$. For more details about the experiment see Section 4.3.2. 4.2.2.

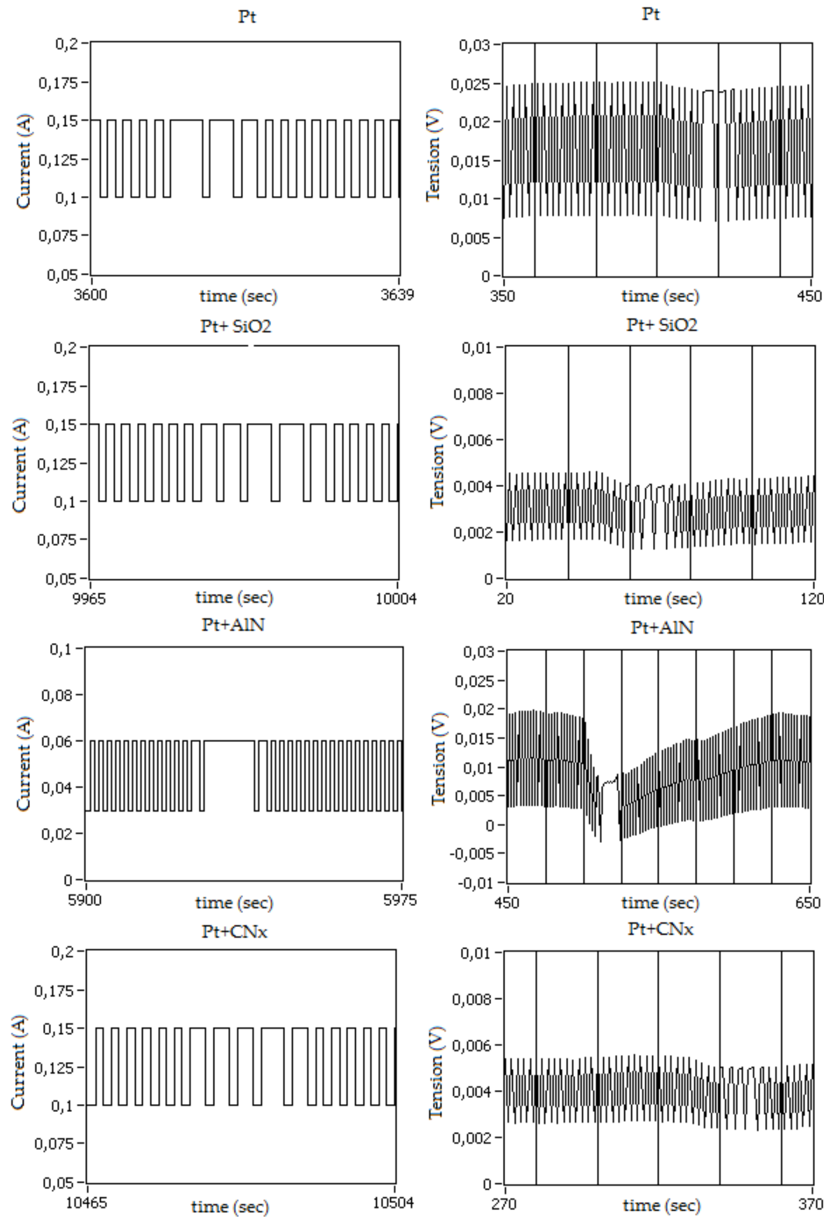

Figure 5.7: The charts at left represent the current oscillation of the CTA setup. At right, the voltage measured at the Wheatstone bridge, which is compared with a threshold value to decide the future state determining the current: $150mA$ when ON and $100mA$ when OFF. This changes in the case of AlN where ON current is $60mA$ and OFF current is $30mA$. Now are enumerated the moment when wind is turned on and when is turned off in each case. Pt:wind on: t=400 wind off: t=420 ,$Pt + SiO_2$:wind on: t=50 wind off: t=70 ,$Pt + AlN$: wind on: t=500 wind off: t=520, $Pt + CN_X$:wind on: t=330 wind off: t=350.

Chapter 6

Summary and Conclusions

The main goal of this work has been to find a material meant to be used as intermediate layer between the platinum film of the anemometer and the surrounding air. Such a material must be electrical isolator in order to not disturb the electrical behavior of the sensor, that is, the electrical resistance of the platinum itself. Otherwise, the additional layer would create a short circuit along the platinum resistance path which would in turn neutralize its main purpose, that is, to linearly vary with wind speed. However some more constraints were present. For instance, the material should be able to be fabricated by sputtering so that it could be deposited in any kind of surface at room temperature. Finally, its merit factor would be its ability to conduct heating well enough in order to reduce as much as possible its thermal inertia thus causing neglecting effects at high working frequencies of the sigma delta converter.

In order to find out physical magnitudes involved in this phenomenon, the anemometer has been modeled by its thermal equivalent circuit assuming distributive effects of the heat flow can be neglected as a first approximation. Hence, a first order low pass filter model composed by a thermal resistance and a thermal capacity (RC) has been chosen.

Although the research began by looking for high conductive materials, it has been revealed, along the research carried out, that time response of a thermal low pass filter, is mainly affected by its thermal diffusivity which is the quotient between the thermal conductivity and the heat capacity, multiplied by the density of the material. Geometry of the material together with this parameter are the variables determining the thermal inertia of the material.

According to this, the bibliographic resources suggested that materials with behavior similar to that of diamond were desired. Among them only a small proportion could be fabricated using the available targets of the sputtering. Fortunately, one the best ones, Aluminum Nitride was theoretically feasible using a target of Aluminum in a rarefied atmosphere of Nitrogen and Argon in order to create the plasma.

Since Silicon Oxide is commonly used as isolator and typical protection layers used in hot wire anemometers are made of this material (quartz coating), it was chosen as well in order to compare at least its behavior to that of the Aluminum Nitride. Moreover, Silicon Oxide is also the substrate used in REMS to propagate thermal flow through the sensor

volume. In addition, Carbon Nitride was also studied because of the high expectancies that this material has arisen in the field of materials engineering due to its expected hardness.

After making various deposits of these materials and characterizing their growth rate, both thermal and electrical experiments has been carried out to compare their thermal and electrical properties.

Main conclusion of these experiments is that a thin layer of Aluminum Nitride is the most suitable material for matching the requirements of the hot film anemometer design. Its thermal conductivity is one of the largest within electrical isolators. Moreover some of the alternatives have serious problems like in the case of Beryllia which is very toxic and its fabrication might be dangerous. After this SiO_2 would be the next option. Although SiO_2 and CN_X behave thermally in a similar way, electrical isolation of SiO_2 is much better probably by more than 6 orders of magnitude (See Section 4.3). In addition sputtering of SiO_2 is a well known procedure and its parameters can be much more controlled. It might well be that no crystal structure has been achieved at all in the Carbon Nitride case. Difficulties with the fabrication of this material have been largely reported in the literature. These results are in agreement with those expected by the works referenced in this report.

Another important conclusion of the experimental research done along the development of the this work is that the material proposed can be and actually have been effectively fabricated without serious problems. This material presents, as expected, very good properties in terms of electrical isolation, which is, in practical terms, similar to that of SiO_2.

Hence all the objectives of this thesis have been successfully achieved. In short these are:

1. A material with the suitable properties has been found: Aluminum Nitride (AlN)
2. It has been successfully fabricated in the clean room by RF Sputtering
3. A close loop validation has been successfully carried out with a hot film anemometer sputtered with the selected material

Indeed, the close loop validation has been successful with all the isolator materials which demonstrates that the solution itself do not disturb the behavior of platinum resistance.

It should be noted however, that all thermal experiments results obtained using the hot plate (See Section 4.2) neglect the effect of the heat losses due to air convection. It might be useful to repeat them in a vacuum chamber to obtain more accurate results. Furthermore, some standard procedure to measure thermal conductivity (such as the *Transient Plane Source method* (TPS)) could be considered in case a quantitative characterization of the materials is needed.

Anyhow, next step in the development of the *MetNet* wind speed sensor should be to sputter the isolating material not in a flat glass but in the real spheric prototype presented in Figure 3.1. Open loop configuration could be useful to check the improvement in performance when compared to the sphere without an isolator layer. In addition, this test could be done in a wind tunnel with an adjustable wind speed so that sensitivity of the

sensor can be measured more accurately. Later on, this experiment could be reproduced in a Martian-like atmosphere.

Later on, as described in Section 3.4 several other improvements are to be investigated yet in order to be able to develop the entire wind sensor that will go onboard the MNL's. These however, fall beyond the scope of the current thesis.

Bibliography

[1] Metnet Official Webside, *http://metnet.fmi.fi*, October 25th, 2009.

[2] E. N. Evlanov, B.V. Zubkov, D.F. Nenarokov, V.N. Linkin, M. A. Zavjalov, *Gas discharge anemometer for the investigation of flow dynamics in rarefied gas media*, 2001, Cosmic Res. 39 (5), 484-490.

[3] J.P. Merrison, H.P. Gunnlaugsson, J. Jensen, K. Kinch, P. Nϕrnberg, K.R. Rasmussen, *A miniature laser anemometer for measurement of wind speed and dust suspension on Mars.* 2004, Planet. Space Sci. 52, 1177-1186.

[4] R. Sullivan, M. Golombek, R. Greeley, K. Herkenhoff, M. Kraft, J. Murphy, P. Smith, G. Wiilson, *Results of the imager for mars pathfinder windsock experiment*, J. Geophys. Res. 105 (E10), 24547-24562.

[5] H.P. Gunnlaugsson, S.K. Jensen, K. Leer, M.B. Madsen, J.P. Merrison, P. Nϕrnberg, M. Olsen, P.I. Smith, *The Telltale wind experiment for the NASA Phoenix Mars Lander 2007*, 2007, EGU.

[6] T.E.Chamberlain, H.L. Cole, R.G. Dutton, G.C. Greene, J.E. Tillman, *Atmospheric measurements on Mars: the Viking meteorology experiment.* 1976, Bull. Am. Meteorol. Soc. 57, 1094-1104.

[7] J. Polkko, A.M. Harri, T. Siili, F. Angrilli, Calcutt S., D. Crisp, S. Larsen, J.M.-P Pommereau, J.M Stoppato, A. Lehto, C. Malique, J.E. Tillman, *The Netlander atmospheric instrument system (ATMIS): description and performance assesment*, 2000, Planet. Space Sci. 48, 1407-1420.

[8] J.T. Schofield, J.R. Barnes, D. Crisp, R.M. Haberle, S. Larsen, J.A. Magalhaes, J.R. Murphy, A. Seiff, G. Wilson, *Investigation/Metereology (ASI/MET) Experiment. The Mars Pathfinder atmospheric structure*, 1997, Science 278, 1752-1757.

[9] M.C. Towner, M.R. patel, T.J. Ringrose, J.C. Zarneki, D. Pullan, M.R. Sims, S. Haapanala, A.-M Harri, J. Polkko, C. Wilson, *The Beagle 2 environmental sensors: science goals and instrument description*, 2004, Planet. Space Sci. 52, 1141-1156.

[10] M.Domínguez, V.Jiménez, J.Ricart, L.Kowalski, J.Torres, S.Navarro, J. Romeral, L. Castañer, *A hot film anemometer for the Martian atmosphere*, 2008, Planet. Space Sci. 56 1169-1179.

[11] M.Domínguez, J. Ricart, A. Moreno, X. Contestí, S. Garriga, *Low cost PCB thermal sigma-delta air flowmeter with improved thermal isolation*, 2005, Sensor Actuators A: Phys. 121, 453-462.

[12] M. Ohring *The Materials Science of Thin Films*, 1992, Academic Press, San Diego, California.

[13] H.H. Bruun *Hot-Wire Anemometry: Principles and Signal Analysis* 1995, Oxford Science Publications.

[14] H. Kramers, *Heat transfer from spheres to flowing media*, 1946, Physica XII(2-3), 61-80.

[15] G. Comte-Bellot, *Hot-wire anemometry.*, 1976, Ann. Rev. Fluid Mech. 8, 209-231.

[16] G.R. Sarma, *Transfer function analysis of the constant voltage anemometer*, 1998, Rev. Sci. Instrum. 69, 2385-2391.

[17] D.C. Collis, M.J. Williams, *Two-dimensional convection from heated wires at low Reynolds numbers*, J. Fluid Mech. 6, 357-384.

[18] Tropea, Yarin, Foss, *Springer Handbook of Experimental Fluid Mechanics*, 2007 Springer.

[19] F. Jiang, Y.C. Tai, C.M. Ho, W. J. Li, *A micromachined Polysilicon Hot-Wire Anemometer*, 1994, EE 116-81, Caltech. CA 91125, USA.

[20] Dantec Dynamics, *Probes for Hot-wire Anemometry*, 2000, Publication No.: 238-v2.

[21] R. Pallás Areny *Sensores y Acondicionadores de Señal*, Marcombo, 4th Edition, 2003.

[22] L.V. King, *On the convection of heat from small cylinders in a stream of fluid: determination of the convection constants of small platinum wires with applications to hot-wire anemometry*, Phil. Trans. Roy. Soc. A214 (1914) 272-432.

[23] W. Xu, T. Fujimoto, B. Li, I. Kojima, *Characterization of the density, structure and chemical states of carbon nitride films*, 2001, National Institute of Materials and Chemical Research, Tsukuba, Ibaraki 305, Japan.

[24] S.L. Shindé, J. Goela *High Thermal Conductivity Materials* 2006, Springer.

[25] G.E. Valley, H. Wallman, *Vacuum Tube Amplifiers*, 1949, MIT Radiation Laboratory Series 18. New York: McGraw-Hill.

[26] S. Goldsmith, E. Çetinörgü, R.L. Boxman, *Modeling the optical properties of tin oxide thin films* 2009, Thin Solid Films 517 (2009) 5146-5160.

[27] G. Leahu, R. Ostuni, E. Tomaselli, M.C. Larciprete, R. Li Voti, C. Sibilia, M. Bertolotti, V. Golubev, D. A.Kurdyukov, C. Lopez, *Study of Thermal and Optical Properties of SiO_2/GaN Opals by Photothermal Deflection Technique* 2006, OSA/IPRA.

[28] H. Chen, J. Zhang, J. Cui, R. Fang, *Deposition of Diamond Film on Aluminum Nitride Ceramics and the Study of Their Thermal Conductance* 1996, Chin. Phys. Lett. Vol. 13, No.8 (1996) 625.

[29] F. Engelmark, G. Fucntes, I.V. Katardjiev, A. Harsta, U. Smith, S. Berg, *Synthesis of highly oriented piezoelectric* AlN *films by reactive sputter deposition*, 2000, American Vacuum Society [S0734-2101(00)09804-3]

[30] Y. Yang, K.A. Nelson *Optical measurement of the elastic moduli and thermal diffusivity of a C-N film* 1994, J. Mater. Res., Vol. 10, No. 1., Materials Research Society.

[31] J. Wei, P. Hing, *Electrical properties of reactively sputtered carbon nitride films* 2002, Thin Solid Films, vol. 410, n°1-2, pp.21-27 (25 ref.)

[32] M. Akiyoshi, I. Takagi, T. Yano, N. Akasaka, Y. Tachi, *Thermal conductivity of ceramics during irradiation* 2006, Fusion Engineering and Design, Vol. 81, Issues 1-7.

[33] F.L. Riley, *Silicon Nitride and Related Materials*, 2000, J. Am. Ceram. Soc., 83 [2] 245-65.

[34] T.L. Pourpoint, R. M. Banish, F. C. Wessling, Robert F. Sekerka *Real-time determination of thermal diffusivity in a disk-shaped sample: Applications to graphite and boron nitride*

[35] G. Yuqin, W. Yajue *An experimental study of thermal resistance of a power semiconductor package* 1988, CH2590-8/88/0000-0037, IEEE.

[36] M. Pecht, R. Agarwal, F. P. McCluskey, T. J. Dishongh, S. Javadpour, R. Mahajan, *Electronic Packagin Materials and Their Properties*, 1998, CRC, 1st Edition.

[37] Z.R. Song, Y.H. Yu, D.S. Shen, S.C. Zou, Z.H. Zheng, E.Z. Luo, Z. Xie, *Dielectric Properties of AlN thin films formed by ion beam enhanced deposition* 2003, Material Letters 57 (2003) 4643 - 4647.

[38] B. Abdallah, A. Chala, P.-Y. Jouna, M.P. Besland, M.A. Djouadi. *Deposition of AlN films by reactive sputtering: Effect of radio frequency substrate bias*, 2007, Thin Solid Films 515 (2007) 7105 - 7108.

[39] V. Dimitrova, D. Manova, E. Valcheva, *Optical and dielectric properties of DC magnetron sputtered AlN thin films correlated with depostion conditions*, 1999, Materials Science and Engineering B68 (1999) 1-4.

[40] J. García López, Y. Morilla, M.A. Respaldiza, M. Clement, E. Iborra, A. Sanz-Hervas, J. Sangrador, *High energy ion characterisation of sputtered AlN thin films* 2003, Diamond and Related Materials 12 (2003) 1157-1161.

[41] A. Y. Liu, M.L. Cohen, *Prediction of new low compressibility solids*, Science 245, 841, 1989.

[42] A. Y. Liu, M.L. Cohen, *Structural properties and electronic structure of low-compressibility materials: $\beta - Si_3N_4$ and hypothetical $\beta - C_3N_4$"*, Phys. Rev. B 41, 10727, 1990.

[43] University of Wisconsin, *Buckyballs, Diamond and Graphite*, `http://www.chem.wisc.edu/~newtrad/CurrRef/BDGTopic/BDGtext/BDGDmnd.html`, 9th September, 2009.

[44] J. Wei, P. Hing *Electrical properties of reactively sputtered carbon nitride films* Thin Solid Films 410 (2002), 21-27, 2002

[45] G. Subodh, M.V. Manjusha, J. Philip, M.T. Sebastian, *Thermal Properties of Polytetrafluoroethylene/$Sr_2Ce_2Ti_5O_{16}$ Polymer/Ceramic Composites*, 2008, Journal of Applied Polymer Science, Vol. 108, 1716-1721.

Appendix A

Virtual Instruments

The Annexes attached here are the virtual instruments, developed in LabView, which have been used to perform the experiments described in the report.

A.1 Thermal Measurements

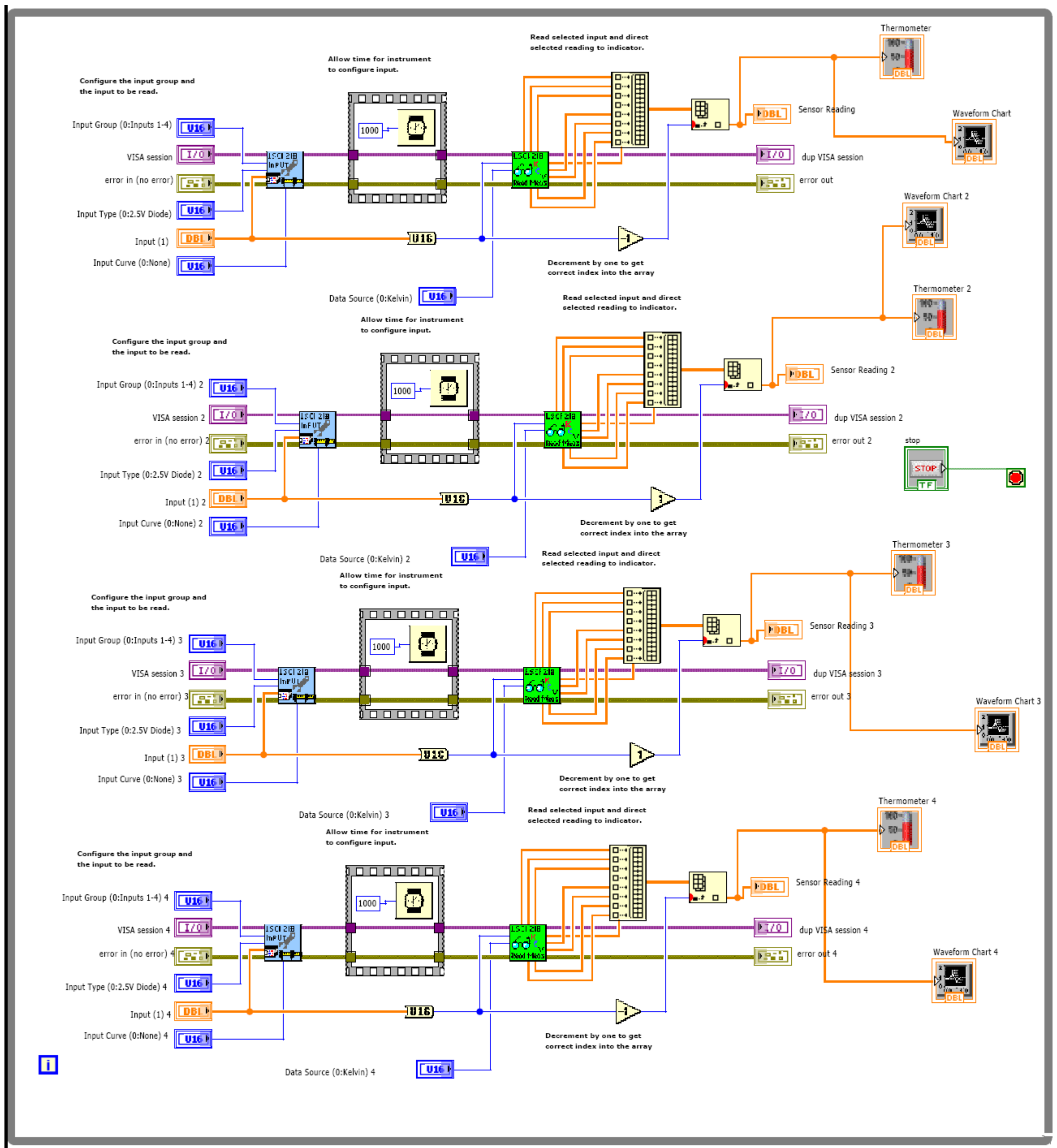

Figure A.1: Virtual Instrument developed in LabView to monitor temperature in experiments explained in Section 4.2.

A.2 Close Loop Validation

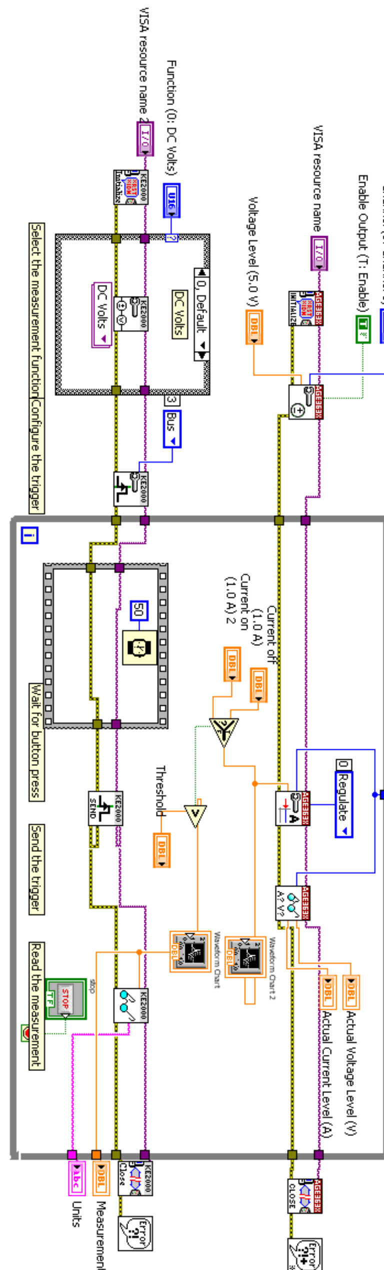

Figure A.2: Virtual Instrument developed in LabView which simulates a sigma delta converter which makes the thermal anemometer to operate in CTA mode. It has been used in Section 4.3.3 to carry out the closed-loop validation.